

Evidence for chiral superconductivity on a silicon surface

Received: 12 August 2022

Accepted: 22 November 2022

Published online: 30 January 2023



F. Ming^{1,12}, X. Wu^{2,3,12}, C. Chen², K. D. Wang²✉, P. Mai⁴, T. A. Maier⁴, J. Stroczko^{5,6}, J. W. F. Venderbos^{5,6}, C. González^{7,8}, J. Ortega⁹, S. Johnston^{10,11}✉ & H. H. Weitering^{10,11}✉

Tin adatoms on a Si(111) substrate with a one-third monolayer coverage form a two-dimensional triangular lattice with one unpaired electron per site. These electrons order into an antiferromagnetic Mott-insulating state, but doping the Sn layer with holes creates a two-dimensional conductor that becomes superconducting at low temperatures. Although the pairing symmetry of the superconducting state is currently unknown, the combination of repulsive interactions and frustration inherent in the triangular adatom lattice opens up the possibility of a chiral order parameter. Here we study the superconducting state of Sn/Si(111) using scanning tunnelling microscopy, scanning tunnelling spectroscopy and quasiparticle interference imaging. We find evidence for a doping-dependent superconducting critical temperature with a fully gapped order parameter, the presence of time-reversal symmetry breaking and a strong enhancement in zero-bias conductance near the edges of the superconducting domains. Although each individual piece of evidence could have a more mundane interpretation, our combined results suggest the possibility that Sn/Si(111) is an unconventional chiral *d*-wave superconductor.

Superconductivity—dissipationless electrical conductivity in conjunction with perfect diamagnetism—is a profound manifestation of a macroscopic quantum phenomenon. Microscopically, supercurrents are carried by Cooper pairs whose pair wave functions become phase locked as they condense, like bosons, into a coherent macroscopic quantum state¹. In conventional superconductors, electron pairing is mediated by virtual phonon exchange. In this case, the relatively slow motion of ions provides a time-retarded effective attractive

interaction that allows the electrons to overcome their mutual repulsion resulting in Cooper pairs with *s*-wave symmetry, where the composite spin and orbital angular momenta of the electrons are zero. Higher-angular-momentum states are typically driven by repulsive interactions^{2,3}, similar to cuprate superconductors with a high critical temperature (T_c) (refs. 3,4). Here electron repulsion is minimized by imposing a nodal structure with a corresponding sign change in the superconducting wave function. More recent emphasis on topological

¹State Key Laboratory of Optoelectronic Materials and Technologies, School of Electronics and Information Technology and Guangdong Province Key Laboratory of Display Material, Sun Yat-sen University, Guangzhou, China. ²Department of Physics, Southern University of Science and Technology, Shenzhen, China. ³School of Physical Sciences, Great Bay University, Dongguan, China. ⁴Computational Sciences and Engineering Division, Oak Ridge National Laboratory, Oak Ridge, TN, USA. ⁵Department of Physics, Drexel University, Philadelphia, PA, USA. ⁶Department of Materials Science and Engineering, Drexel University, Philadelphia, PA, USA. ⁷Departamento de Física de Materiales, Universidad Complutense de Madrid, Madrid, Spain. ⁸Instituto de Magnetismo Aplicado, UCM-ADIF, Madrid, Spain. ⁹Departamento de Física Teórica de la Materia Condensada and Condensed Matter Physics Center (IFIMAC), Facultad de Ciencias, Universidad Autónoma de Madrid, Madrid, Spain. ¹⁰Department of Physics and Astronomy, The University of Tennessee, Knoxville, TN, USA. ¹¹Institute of Advanced Materials and Manufacturing, The University of Tennessee, Knoxville, TN, USA. ¹²These authors contributed equally: F. Ming, X. Wu. ✉e-mail: wangkd@sustech.edu.cn; sjohn145@utk.edu; hanno@utk.edu

materials systems has raised expectations for the discovery of novel multicomponent order parameters that are topologically distinct from those of ordinary Cooper-pair condensates^{5–15}. Besides the microscopic nature of pairing interactions, the physics of these systems is dictated by broken symmetries such as crystal, spin rotation and time-reversal symmetries, although the experimental validation of intrinsically topological order parameters remains scant.

Superconductivity has recently been discovered in a system comprising one-third monolayer of Sn deposited on degenerately doped p-type Si(111) substrates¹⁶. Its pairing symmetry, however, remains undetermined. This system is of particular interest because the undoped Sn monolayer is an antiferromagnetic single-band Mott insulator^{17–19} that becomes superconducting on hole doping, drawing interesting comparisons with high- T_c cuprates^{3,20} with d -wave order parameters. The Sn layer, however, has triangular-lattice symmetry imposed by the Si(111) substrate. This geometry naturally allows for the existence of a chiral order parameter with topological edge states^{7,12,21}, if repulsive interactions dominate the pairing. The appearance of such an exotic order parameter is expected to furthermore depend on the electron correlation strength, shape of the Fermi surface and doping level^{7,21,22}. In particular, recent renormalization group calculations for the Sn/Si(111) system indicated a competition between chiral d - and f -wave instabilities and triplet p -wave instabilities, depending on the doping level and value of the nearest-neighbour Hubbard repulsion²². At the same time, electron–phonon interactions, particularly to interfacial Si modes²³, could drive a conventional s -wave pairing¹⁶.

Here we study the superconducting state of the Sn/Si(111) interface using scanning tunnelling microscopy (STM), scanning tunnelling spectroscopy (STS) and quasiparticle interference (QPI) imaging. Our observations reveal a strong doping dependence of a superconducting T_c , a fully gapped order parameter, the presence of time-reversal symmetry breaking and a strong enhancement in zero-bias conductance near the edges of the superconducting domains. Although each of these observations may have a mundane explanation, we discuss why we believe that a chiral d -wave scenario offers the most consistent interpretation of the measurements and theoretical modelling. Final confirmation, however, awaits experimental validation concerning the topological nature of the edge-state conductance.

At one-third monolayer coverage, the Sn adatoms form a ($\sqrt{3} \times \sqrt{3}$) superlattice on the Si(111) surface with one half-filled dangling-bond orbital per site and a Sn–Sn distance of 6.65 Å (Fig. 1a). All the other chemical bonds in the system are passivated. The non-interacting dangling-bond surface state has a bandwidth $W \approx 0.50$ eV (Fig. 1b), which is comparable to the onsite Hubbard interaction $U \approx 0.66$ eV of the dangling-bond orbitals¹⁸. As such, the system is a Mott insulator with an upper Hubbard band (UHB) and lower Hubbard band (LHB) straddling the Fermi level (Fig. 1c).

Figure 1d shows an STM image of the triangular Sn adatom lattice. The Sn atoms are clearly resolved and well ordered. The dark point defects correspond to substitutional Si adatoms (most prevalent) and Sn adatom vacancies. Holes are introduced via modulation doping, using boron-doped Si substrates with different doping levels^{16,19} (Supplementary Note 1 and Supplementary Fig. 1 provide a discussion on dopant segregation). The hole concentration in the dangling-bond surface state is estimated from the spectral weight transfer in the tunnelling spectra, associated with the introduction of holes and formation of a quasiparticle peak in the Mott gap (Fig. 1b and Extended Data Fig. 1)¹⁹.

Figure 1e shows the normalized dI/dV tunnelling spectra for excess hole concentrations of $p = 0.06$, 0.08 and 0.10, recorded at $T = 0.5$ K (the data for $p = 0.10$ are reported elsewhere¹⁶). These spectra are representative of the superconducting density of states (DOS). Here we divided the raw tunnelling spectra by the normal-state dI/dV spectrum obtained in a perpendicular 15 T magnetic field. This field is large enough to completely suppress the superconductivity for the $p = 0.08$ and 0.10 samples, which have upper critical field values of $H_{c2}(0.5\text{ K})$ of

3 T (ref. ¹⁶) and 13 T, respectively (Extended Data Fig. 2). This procedure is a bit problematic for the $p = 0.06$ sample, where the upper critical field exceeds the magnetic-field capability of our instrument (15 T).

The Sn adatom lattice (Fig. 1a) is highly ordered, whereas the boron dopants are located in the silicon bulk. The superconducting DOS is, therefore, spatially uniform away from the localized point defects and edges of the ($\sqrt{3} \times \sqrt{3}$) domains. Figure 1f shows a series of spectra recorded at $T = 0.5$ K along the line segment shown in Fig. 1d. This level of homogeneity distinguishes Sn in the Si(111) system from, for example, complex oxides, which exhibit considerable electronic inhomogeneity, often in conjunction with various competing orders^{24,25}.

The normalized dI/dV spectra of the $p = 0.08$ sample are plotted as a function of temperature (Fig. 1g). The gap feature persists up to about 8 K. Detailed Dynes fits²⁶ of the spectra assuming s -wave and $d_{x^2-y^2} \pm id_{xy}$ order parameter symmetries, as well as zero-bias conductance measurements as a function of temperature, consistently produce T_c of about 7.6 ± 0.2 K with some evidence of superconducting fluctuations above T_c (ref. ¹⁶, Extended Data Fig. 3 and Fig. 2a). A similar procedure for the $p = 0.10$ sample produces $T_c = 4.7 \pm 0.3$ K (ref. ¹⁶), whereas T_c of the $p = 0.06$ sample was difficult to ascertain because the spectra cannot be properly normalized ($H_{c2}(0.5\text{ K}) > 15\text{ T}$). We conservatively estimate its T_c to be around 9 K (Extended Data Fig. 2).

Fitting the $p = 0.08$ dI/dV spectra with an s -wave gap produces a reasonable fit but with notable discrepancies near zero bias. Turning to potential chiral order parameters, we find that a chiral d -wave fit also agrees well with the data and even improves the fit at lower energies. A chiral p -wave gap clearly fails to describe the spectra, particularly at low energy (Fig. 2a). This failure occurs because any p -wave gap function must vanish at the M point by symmetry. This point corresponds to the Van Hove singularity and lays close to the Fermi surface^{16,19}. Therefore, it affects the gap substantially, producing pronounced shoulders in the DOS that are not experimentally observed. Other parameter symmetries such as extended chiral p -wave and nematic d -wave symmetries (that is, $d_{x^2-y^2}$ and d_{xy}) do not fit the spectra either (Supplementary Note 2 and Supplementary Fig. 2) (a multigap order parameter can also be ruled out since this is a single-band system). Only s -wave and chiral d -wave symmetries produce good results, and it is not possible to conclusively discriminate between the two based on fitting alone.

Important details about the Fermi surface and order parameter symmetry can be obtained from spectroscopic STM imaging²⁷. Here one acquires a spatial map of the differential tunnelling conductance $g(\mathbf{r}, V) = dI(\mathbf{r}, V)/dV$. Such dI/dV maps typically reveal the presence of electronic standing waves as quasiparticles are elastically scattered by defects on the surface. The power spectrum of the differential conductance map—the QPI spectrum—then identifies the dominant scattering processes contributing to the standing-wave pattern. In itinerant systems, these typically correspond to scattering wavevectors connecting different \mathbf{k} points on constant-energy contours (corresponding to imaging bias) $\mathbf{q} = 2\mathbf{k} \pm \mathbf{G}$, where \mathbf{G} is a reciprocal lattice vector of the ($\sqrt{3} \times \sqrt{3}$) adatom lattice.

Figure 2b,c shows the $T = 0.5$ K QPI spectra taken at ± 5 meV bias ($p = 0.08$). Both spectra reveal the warped hexagonal Fermi contour of the normal state ($\mathbf{G} = 0$), highlighted in magenta, along with several scattering replicas ($\mathbf{G} \neq 0$), as indicated by the light-blue dumbbell-shaped contours¹⁹. These spectra agree very well with previous calculations for the spectra in the normal state, and are fully consistent with the band structure for the Sn surface state¹⁹ (the presence of the quasiparticle band and its dispersion is inconsistent with an interpretation in terms of impurity band physics; Supplementary Note 3 and Supplementary Fig. 3). Real-space differential conductance maps at zero bias (Fig. 2d), that is, deep inside the superconducting gap, reveal the existence of very strong star-like scattering features centred at the various surface defects. The corresponding Fourier map (Fig. 2e) now reveals the presence of a flower-like feature centred at

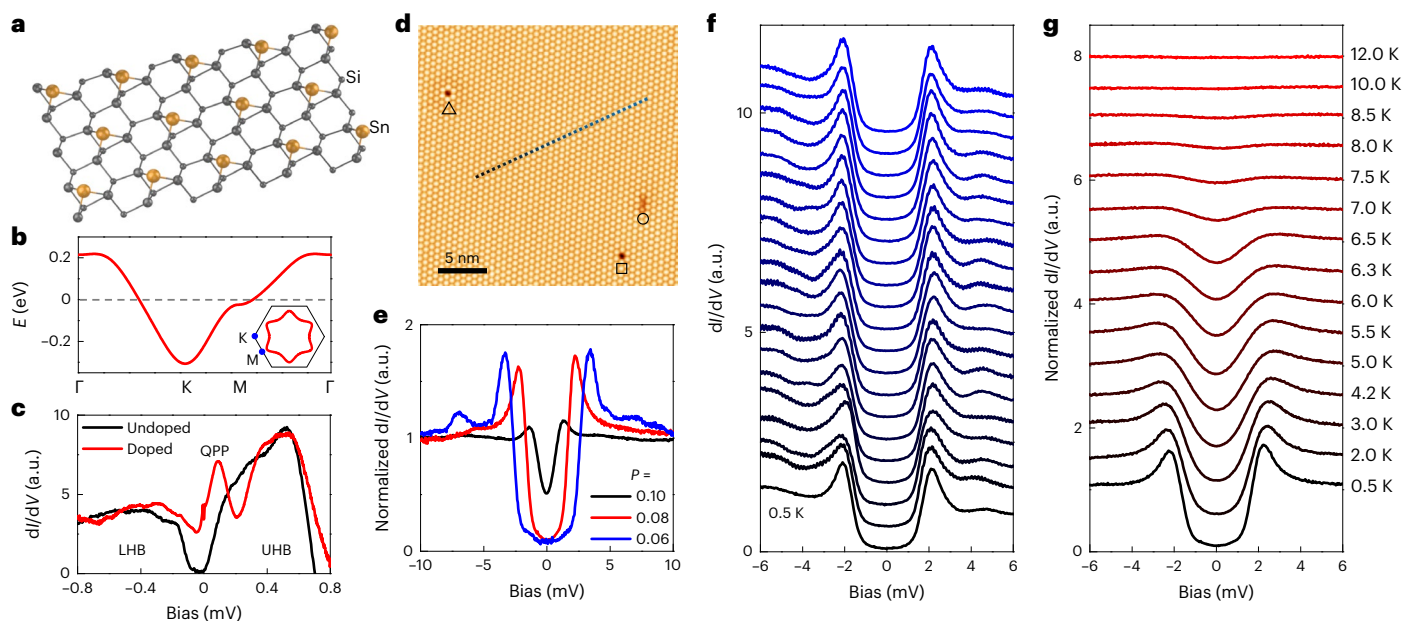


Fig. 1 | Structure, topography and spectral properties of the superconducting $(\sqrt{3} \times \sqrt{3})$ -Sn surface on Si(111). **a**, Structure model with the three outermost surface layers and one Sn adatom per $(\sqrt{3} \times \sqrt{3})$ unit cell. **b**, Non-interacting dispersion of the dangling-bond surface state¹⁸. The inset shows the Fermi surface in the hexagonal-surface Brillouin zone. The high-symmetry points are indicated. The Γ point is located at the centre of the hexagon. **c**, Comparison of differential conductance spectra of two Si(111)/ $(\sqrt{3} \times \sqrt{3})$ -Sn surfaces. The spectrum for the undoped surface¹⁶, acquired at 77 K, showing UHB and LHB as well as a small gap around the Fermi level; the other spectrum is from

a doped surface ($p = 0.08$) obtained at 0.5 K, showing an extra quasiparticle peak (QPP) near the Fermi level¹⁶. **d**, Topographic STM image ($V_t = -0.1$ V, $I_t = 0.1$ nA) showing a near-perfect Sn adatom lattice, along with a substitutional Si defect, vacancy and other defects, labelled with a triangle, square and circle, respectively ($p = 0.08$). **e**, Normalized STS spectra for three different hole concentrations, revealing a clear doping dependence of the superconducting gap. **f**, A set of raw dI/dV spectra taken at equidistant locations along the dotted line shown in **d**, starting on the left ($p = 0.08$). **g**, Normalized dI/dV spectra as a function of temperature ($p = 0.08$). The spectra in **f** and **g** are vertically offset for clarity.

$q = 0$ and with six ‘petals’ pointing towards the Bragg points of the $(\sqrt{3} \times \sqrt{3})$ lattice, as outlined by the red contour. Meanwhile, the Fermi contour seen at ± 5 meV is suppressed. This flower-like feature appears to be intimately related to the superconductivity; it only exists when the sample is in the superconducting state (Fig. 3a,b) and when the tunnelling bias is within the superconducting gap (Fig. 2b,c,e). Hence, they are unique features of the superconducting state (Extended Data Fig. 4 shows additional QPI results).

To elucidate the origin of flower-like features, we first simulated the QPI patterns for the s -wave and chiral d -wave order parameters using the T-matrix formalism and assuming non-magnetic scattering (Methods). Figure 3 shows the experimental QPI spectra of the $p = 0.10$ sample, along with the simulated spectra for the $d_{x^2-y^2} \pm id_{xy}$ and s -wave state. The experimental pattern (Fig. 3b) is well reproduced in the calculations for the d -wave pairing channel (Fig. 3c) (the theoretical features exhibit much more curvature because the calculations are based on non-interacting band dispersion, whereas experimental band dispersion has correlation-driven band renormalizations¹⁹). Importantly, the flower is absent for the s -wave (both isotropic and anisotropic) pairing channel (Fig. 3d).

Our simulations reveal that the flower-like features only appear when time-reversal symmetry is broken. Such would be the case for non-magnetic scattering in a chiral superconductor, as simulated above, but it could also be due to magnetic scattering in an s -wave superconductor (Extended Data Fig. 5). In particular, the star-like scattering features in the real-space QPI maps are very similar to those observed for magnetic point scatterers in s -wave systems, and have been attributed to a focusing effect of magnetic bound states or Yu–Shiba–Rusinov (YSR) states due to Fermi surface anisotropy^{28–32}. To discriminate between the s -wave and d -wave scenarios, it is essential to establish the nature of defects on the surface.

The most prevalent scattering defect on the surface is the substitutional Si adatom (replacing a Sn adatom). It shows up as a dark void in filled-state STM images and as a depressed adatom in the empty-state images (Extended Data Fig. 6). This observation indicates that the sp_z -like dangling-bond orbital of the Si atom is empty; also, because the adatom forms three covalent backbonds with the Si substrate, the Si adatom is expected to be non-magnetic. This is confirmed via first-principles density functional theory (DFT) total-energy calculations (which show that Si adatoms are placed 0.6 Å below the Sn adatoms) and by STM image simulations (Methods and Extended Data Fig. 6). In addition, spin-polarized DFT calculations (Methods) confirm the non-magnetic nature of this defect.

It is not possible to ascertain the nature of all the native defects on the surface (Extended Data Fig. 7a) and thus rule out any magnetic scattering contribution to the QPI pattern. We, therefore, created a new type of defect by depositing a tiny excess amount of (non-magnetic) Sn atoms at 120 K. STM images indicate that additional Sn adatoms are located at three-fold symmetric interstitial adatom sites, surrounded by three Sn adatoms of the two-dimensional host lattice (Extended Data Fig. 6). The excess Sn atoms easily move under the STM tip at tunnelling biases in excess of ± 0.8 V, indicating that they are weakly bound to the surface. The interstitial adatom location is validated by DFT total-energy minimization and STM image simulations. In particular, notice the excellent agreement between the experimental and theoretical STM images (Extended Data Fig. 6). This level of agreement gives us confidence that the calculations correctly capture the local electronic structure. Importantly, spin-polarized DFT indicates that these defect centres are also non-magnetic. The latter can be understood from the fact that the interstitial Sn atom and its three nearest neighbours have negligible contribution to the DOS at the Fermi level (Extended Data Fig. 6), thus pre-empting a potential magnetic instability.

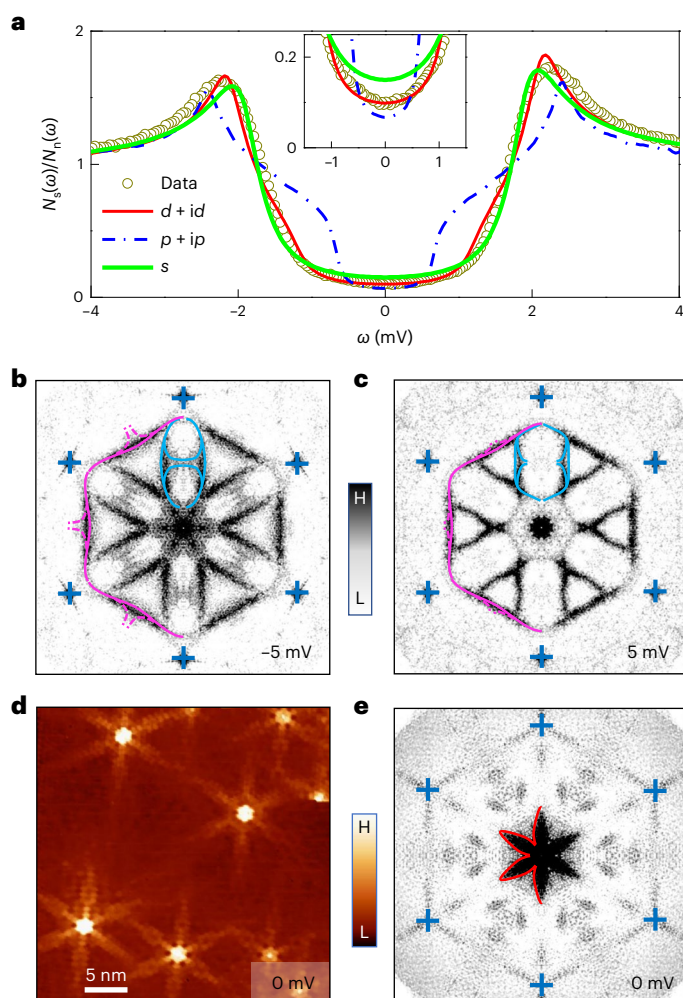


Fig. 2 | Low-temperature differential conductance and QPI spectra of the $(\sqrt{3} \times \sqrt{3})$ -Sn surface ($p = 0.08$) on Si(111). a, Best fits of the low-energy normalized dI/dV spectra at $T = 0.5$ K for different pairing symmetries. The inset shows a zoomed-in view of the zero-bias region. **b, c**, QPI images acquired at $V_s = -5$ mV (**b**) and $V_s = +5$ mV (**c**) beyond the superconducting gap. **d**, Real-space conductance map $g(\mathbf{r}, V)$, obtained at zero bias. The bright six-leaf features are scattering features from surface defects. **e**, Corresponding QPI spectrum $g(\mathbf{q}, V)$ obtained from the conductance map in **d** via Fourier transformation. The six dark-blue crosses in **b**, **c** and **e** indicate the Bragg peaks, whereas the coloured contours highlight the characteristic features in each QPI image.

Figure 4a plots the STS spectra across a substitutional Si defect, which reveals the existence of two in-gap states ($p = 0.08$). These states appear in pairs located symmetrically about the Fermi level reminiscent of YSR bound states, although the substitutional defect is non-magnetic. All the defects on the surface we have checked produce these YSR-like in-gap states but at different energies, including the native vacancy defects, interstitial Si, excess Sn adatoms and various other defects (Extended Data Fig. 7). This is to be expected in a chiral d -wave scenario because both potential and magnetic defects are pair breaking^{33,34}. In the s -wave scenario, on the other hand, one would have to assume that all these defects are magnetic³⁵, which seems unlikely (Extended Data Fig. 5). Interestingly, the non-magnetic interstitial Sn adatoms produce the strongest star-like scattering features in real-space QPI maps and the most intense flower-like features in the corresponding power spectrum (Extended Data Fig. 7e–g). These enhanced scattering features near the excess Sn adatoms suggest that the s -wave scenario can be dismissed because time-reversal symmetry

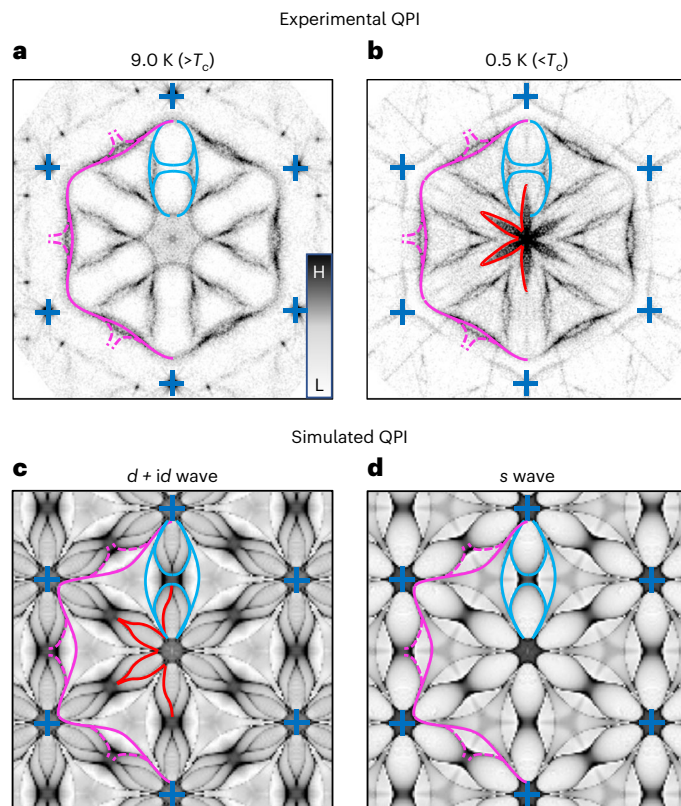


Fig. 3 | Comparison of the measured QPI spectra with theory. a, b, Experimental QPI images $g(\mathbf{q}, V)$ obtained at zero bias on the $p = 0.10$ surface above (**a**) and below T_c (**b**). **c, d**, Simulated QPI images for a superconductor with a chiral d -wave (**c**) and s -wave (**d**) order parameter, assuming non-magnetic defects. In each image, the six dark-blue crosses indicate the locations of Bragg points, whereas the coloured contours highlight the characteristic features in each QPI spectrum.

should not be broken in such a case. Alternatively, one might suggest that non-magnetic impurities are present in a magnetically ordered background, where they behave as magnetic impurities. Such a scenario, however, would require coexisting magnetism and superconductivity and point towards an unconventional order parameter (Supplementary Note 4).

Theory predicts^{33,34} that the bound states of strong scatterers will be located deeper inside the gap compared with those of weaker scatterers. Indeed, we find that the substitutional Si defects produce in-gap states at ± 0.6 meV, whereas interstitial Sn atoms produce states at ± 0.2 meV. Note that the existence of gap states alone for each and every scattering defect is an indication of unconventional (that is, non- s -wave) superconductivity.

Our experimental measurements thus far point to a chiral d -wave superconducting state. To demonstrate that this pairing symmetry is consistent with the known electronic structure, we performed quantum Monte Carlo dynamical cluster approximation (DCA) method^{36,37} calculations for the leading pairing instability of the $(\sqrt{3} \times \sqrt{3})$ -Sn system. Here we consider a 3×3 triangular-lattice single-band Hubbard cluster embedded in a dynamical mean field and adopt parameters previously used to describe doped¹⁹ and undoped¹⁸ $(\sqrt{3} \times \sqrt{3})$ Sn (Methods). Since our calculations are limited by the fermion sign problem, we focused on doping levels of $p = 0.05, 0.10$ and 0.15 , where we are able to access temperatures as low as $T = 6.59$ meV ($\beta t_f = 8$). For these parameters, the dominant superconducting instability indeed corresponds to degenerate $d_{x^2-y^2}$ and d_{xy} order parameters at all the doping levels (Extended Data Fig. 8). These results are consistent not only with our observations but also several prior studies for the triangular-lattice Hubbard^{21,38} and

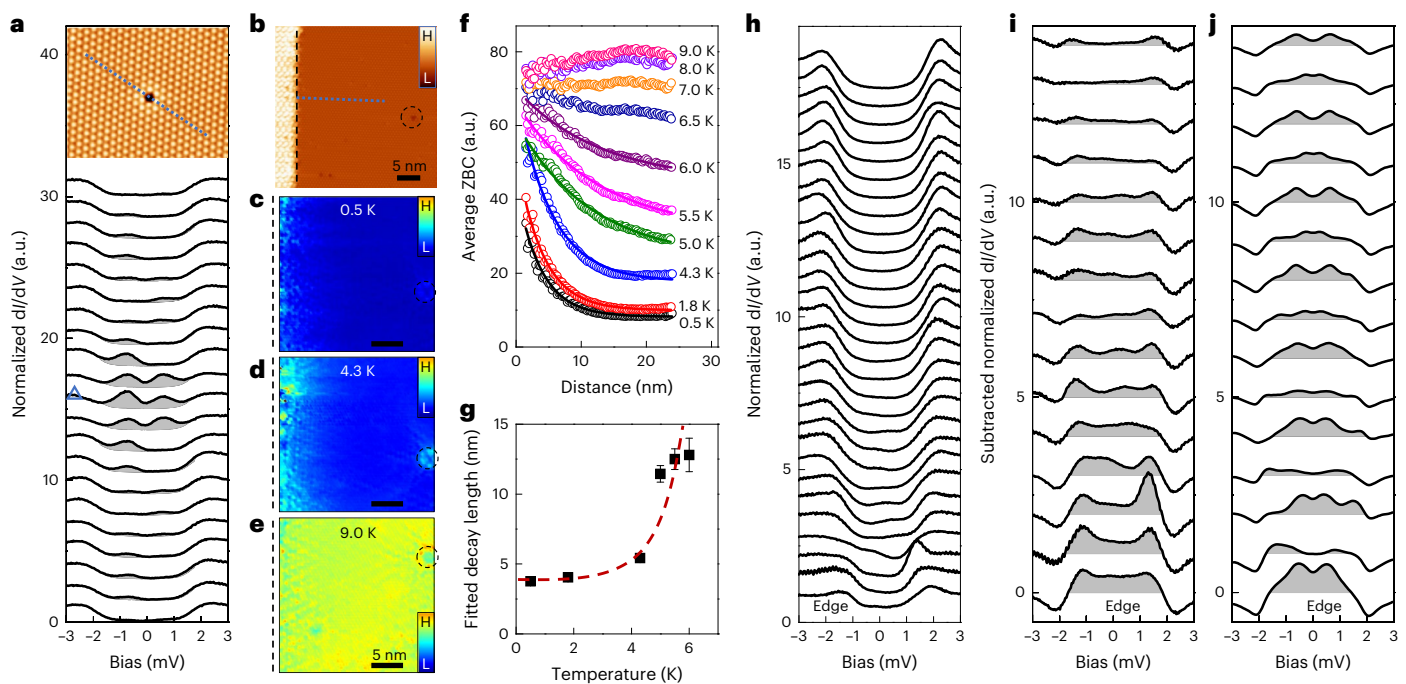


Fig. 4 | Defect states and edge states on the $(\sqrt{3} \times \sqrt{3})$ -Sn surface ($p = 0.08$). **a**, STS point spectra (0.5 K) for each Sn atom along the blue dotted line in the topographic image ($V_s = 0.5$ V, $I_t = 1$ nA) at the top with a substitutional Si defect in the middle. The bottom spectrum corresponds to the left end of the line. The spectrum recorded right on top of the defect is indicated by a triangle. The spectra near the defect site exhibit two gap states at $E_B = \pm 0.6$ meV. **b**, A $(\sqrt{3} \times \sqrt{3})$ -Sn superconducting domain ($V_s = 0.8$ V, $I_t = 0.1$ nA) next to a semiconducting Si(111)($2\sqrt{3} \times 2\sqrt{3}$)R30°-Sn domain on the far-left side of the image (bright strip). **c–e**, Registry-aligned real-space conductance maps $g(\mathbf{r}, V = 0$ mV) of the $(\sqrt{3} \times \sqrt{3})$ -Sn domain measured at temperatures of 0.5 K (**c**), 4.3 K (**d**) and 9.0 K (**e**). In **b–e**, the vertical dashed lines label the domain boundary and the dashed circles label the locations of the same defect. **f**, Averaged zero-bias conductance (ZBC) as a function of distance from the domain boundary. Each line is obtained

from a conductance map $g(\mathbf{r}, V = 0$ mV), recorded at the indicated temperature. The first six curves are fitted with an exponential decay. **g**, Fitted decay lengths as a function of temperature. The dashed line is a guide to the eye. The error bars indicate the uncertainty of the fittings. **h**, STS spectra taken at 0.5 K along the dotted line in **b**, starting at the domain boundary on the left. **i**, The 15 bottom-most spectra from **h** after subtracting the dI/dV spectrum recorded deep inside the $(\sqrt{3} \times \sqrt{3})$ domain. These spectra highlight the edge-state contribution (indicated by shading) to the measured dI/dV spectra. **j**, Simulated DOS of a chiral $d + id$ superconductor, approaching the open edge of a cylinder (Methods). As in **i**, a spectrum from the centre of the cylinder is subtracted to highlight the contribution from the edge state to the total DOS inside the superconducting gap. The spectra in **h–j** are vertically shifted for clarity.

t - J models³⁹ and a recent renormalization group study for Sn/Si(111) that found chiral p -, d - and f -wave pairing symmetries depending on the doping level and value of the nearest-neighbour Hubbard repulsion V (ref. 22), with chiral d -wave pairing becoming dominant when V is small. We also find that the strength of the chiral d -wave pairing correlations increases as the doping level decreases, consistent with observed gap magnitudes (Fig. 1e).

Our experimental and theoretical results are so far consistent with chiral d -wave pairing. Such a pairing state should be characterized by a topological invariant⁴⁰, given by Chern number of 2 (ref. 41). Given the non-trivial topology of the bulk pairing state, we expect the presence of chiral edge modes on sample boundaries⁴², but do not expect unpaired zero energy Majorana bound states at the centre of a vortex core, which arise in the case of effectively spinless $p + ip$ pairing⁵. Indeed, we find no evidence for a Majorana zero mode at the centre of a vortex core (Extended Data Fig. 9). We did, however, find evidence consistent with the presence of chiral edge modes (Fig. 4b–i).

Figure 4b shows a topographic map near a domain wall (vertical dashed line) between the superconducting $(\sqrt{3} \times \sqrt{3})$ domain on the right and semiconducting $(2\sqrt{3} \times 2\sqrt{3})$ domain⁴³ on the left. Figure 4c,d shows the registry-aligned zero-bias conductance maps over the same region of the sample as a function of temperature. The data reveal a region of increased conductance that penetrates the $(\sqrt{3} \times \sqrt{3})$ domain, consistent with the presence of an edge state, which grows as the temperature increases. To estimate the penetration length, we averaged the zero-bias conductance along the vertical direction

and plotted it as a function of distance towards the interior (Fig. 4f). The data in the superconducting state are reasonably well described by an exponential decay (Fig. 4f, solid black lines), and we estimate that the decay length grows from ≈ 3.8 nm at $T = 0.5$ K to ≈ 12.8 nm at 6.0 K.

The increased zero-bias conductance can also be seen in the individual dI/dV spectra (Fig. 4h) taken along the line approaching the domain boundary. To highlight the DOS contribution emanating from the edge, we subtracted a dI/dV spectrum taken from deep in the bulk from the spectra in Fig. 4h (Fig. 4i). The data show that the superconducting coherence peaks shift to lower energies when the edge is approached, as indicated by the formation of the peak–dip structures at about ± 2.2 mV in the subtracted spectra. At the same time, the spectral weight in the superconducting gap increases almost uniformly as a function of energy. This behaviour is consistent with an overlapping DOS from a linearly dispersing edge mode. To confirm this, we computed the chiral edge modes from a simple chiral d -wave mean-field model defined on a cylinder with open-boundary conditions (Methods and Extended Data Fig. 10). The simulated subtracted data, analogous to the data in Fig. 4i, are shown in Fig. 4j where they qualitatively reproduce the experimental data. We note, however, that our non-interacting model has some additional substructure in the DOS for the edge state, which arise from the spatial structure of the edge-state wave function. Although we also observe the substructure in the experimental spectra, the details somewhat differ from theory. We expect that a detailed analysis of these features will require the inclusion of interactions in our edge-state model, which we leave for

future work. Although the enhanced zero-bias edge conductance is consistent with the presence of an edge mode, it is difficult to disentangle possible contributions from traditional coherence length effects (or inverse proximity effects⁴⁴). Also, the evidence does not imply that the edge-state conductance is topological in nature, which will be hopefully elucidated in future studies. Nevertheless, our combined results suggest the possibility that the hole-doped Sn/Si(111) Mott insulator system is an unconventional chiral *d*-wave superconductor.

The Sn/Si(111) system may not be unique. Many semiconductor surfaces and interfaces can be viewed as two-dimensional dangling-bond lattices or narrow-band systems that are inherently unstable towards structural distortion and electronic rearrangement⁴⁵. The modulation doping approach employed in this study can probably unveil novel competing orders and/or topological phases on easily accessible semiconductor templates.

Online content

Any methods, additional references, Nature Portfolio reporting summaries, source data, extended data, supplementary information, acknowledgements, peer review information; details of author contributions and competing interests; and statements of data and code availability are available at <https://doi.org/10.1038/s41567-022-01889-1>.

References

- Bardeen, J., Cooper, L. N. & Schrieffer, J. R. Theory of superconductivity. *Phys. Rev.* **108**, 1175–1204 (1957).
- Kohn, W. & Luttinger, J. M. New mechanism for superconductivity. *Phys. Rev. Lett.* **15**, 524–526 (1965).
- Scalapino, D. J. A common thread: the pairing interaction for unconventional superconductors. *Rev. Mod. Phys.* **84**, 1383–1417 (2012).
- Tsuei, C. C. & Kirtley, J. R. Pairing symmetry in cuprate superconductors. *Rev. Mod. Phys.* **72**, 969–1016 (2000).
- Read, N. & Green, D. Paired states of fermions in two dimensions with breaking of parity and time-reversal symmetries and the fractional quantum Hall effect. *Phys. Rev. B* **61**, 10267–10297 (2000).
- Joynt, R. & Taillefer, L. The superconducting phases of UPT₃. *Rev. Mod. Phys.* **74**, 235–294 (2002).
- Nandkishore, R., Levitov, L. S. & Chubukov, A. V. Chiral superconductivity from repulsive interactions in doped graphene. *Nat. Phys.* **8**, 158–163 (2012).
- Kallin, C. Chiral *p*-wave order in Sr₂RuO₄. *Rep. Prog. Phys.* **75**, 042501 (2012).
- Black-Schaffer, A. M. Edge properties and Majorana fermions in the proposed chiral *d*-wave superconducting state of doped graphene. *Phys. Rev. Lett.* **109**, 197001 (2012).
- Kiesel, M. L., Platt, C., Hanke, W. & Thomale, R. Model evidence of an anisotropic chiral *d*+*id*-wave pairing state for the water-intercalated Na_xCoO₂·*y*H₂O superconductor. *Phys. Rev. Lett.* **111**, 097001 (2013).
- Black-Schaffer, A. M. & Honerkamp, C. Chiral *d*-wave superconductivity in doped graphene. *J. Phys. Condens. Matter* **26**, 423201 (2014).
- Kallin, C. & Berlinsky, J. Chiral superconductors. *Rep. Prog. Phys.* **79**, 054502 (2016).
- Mackenzie, A. P., Scaffidi, T., Hicks, C. W. & Maeno, Y. Even odder after twenty-three years: the superconducting order parameter puzzle of Sr₂RuO₄. *npj Quantum Mater.* **2**, 40 (2017).
- Pustogow, A. et al. Constraints on the superconducting order parameter in Sr₂RuO₄ from oxygen-17 nuclear magnetic resonance. *Nature* **574**, 72–75 (2019).
- Jiao, L. et al. Chiral superconductivity in heavy-fermion metal UTe₂. *Nature* **579**, 523–527 (2020).
- Wu, X. et al. Superconductivity in a hole-doped Mott-insulating triangular adatom layer on a silicon surface. *Phys. Rev. Lett.* **125**, 117001 (2020).
- Schuwallow, S., Grieger, D. & Lechermann, F. Realistic modeling of the electronic structure and the effect of correlations for Sn/Si(111) and Sn/Ge(111) surfaces. *Phys. Rev. B* **82**, 035116 (2010).
- Li, G. et al. Magnetic order in a frustrated two-dimensional atom lattice at a semiconductor surface. *Nat. Commun.* **4**, 1620 (2013).
- Ming, F. et al. Realization of a hole-doped Mott insulator on a triangular silicon lattice. *Phys. Rev. Lett.* **119**, 266802 (2017).
- Lee, P. A., Nagaosa, N. & Wen, X.-G. Doping a Mott insulator: physics of high-temperature superconductivity. *Rev. Mod. Phys.* **78**, 17–85 (2006).
- Cao, X. et al. Chiral *d*-wave superconductivity in a triangular surface lattice mediated by long-range interaction. *Phys. Rev. B* **97**, 155145 (2018).
- Wolf, S., Di Sante, D., Schwemmer, T., Thomale, R. & Rachel, S. Triplet superconductivity from nonlocal Coulomb repulsion in an atomic Sn layer deposited onto a Si(111) substrate. *Phys. Rev. Lett.* **128**, 167002 (2022).
- Zahedifar, M. & Kratzer, P. Phonon-induced electronic relaxation in a strongly correlated system: the Sn/Si(111) ($\sqrt{3} \times \sqrt{3}$) adlayer revisited. *Phys. Rev. B* **100**, 125427 (2019).
- Howald, C., Eisaki, H., Kaneko, N. & Kapitulnik, A. Coexistence of periodic modulation of quasiparticle states and superconductivity in Bi₂Sr₂CaCu₂O_{8+δ}. *Proc. Natl Acad. Sci. USA* **100**, 9705–9709 (2003).
- Vershinin, M. et al. Local ordering in the pseudogap state of the high-*T_c* superconductor Bi₂Sr₂CaCu₂O_{8+δ}. *Science* **303**, 1995–1998 (2004).
- Dynes, R. C., Narayanamurti, V. & Garno, J. P. Direct measurement of quasiparticle-lifetime broadening in a strong-coupled superconductor. *Phys. Rev. Lett.* **41**, 1509–1512 (1978).
- Petersen, L., Hofmann, P., Plummer, E. W. & Besenbacher, F. Fourier transform-STM: determining the surface Fermi contour. *J. Electron. Spectrosc. Relat. Phenom.* **109**, 97–115 (2000).
- Yu, L. Bound state in superconductors with paramagnetic impurities. *Acta Phys. Sin.* **21**, 75 (1965).
- Shiba, H. Classical spins in superconductors. *Prog. Theor. Phys.* **40**, 435–451 (1968).
- Rusinov, A. I. Superconductivity near a paramagnetic impurity. *JETP Lett.* **9**, 85–87 (1969).
- Ménard, G. C. et al. Coherent long-range magnetic bound states in a superconductor. *Nat. Phys.* **11**, 1013–1016 (2015).
- Kim, H., Rózsa, L., Schreyer, D., Simon, E. & Wiesendanger, R. Long-range focusing of magnetic bound states in superconducting lanthanum. *Nat. Commun.* **11**, 4573 (2020).
- Wang, Q.-H. & Wang, Z. D. Impurity and interface bound states in $d_{x^2-y^2} \pm id_{xy}$ and $p_x \pm ip_y$ superconductors. *Phys. Rev. B* **69**, 092502 (2004).
- Mashkooi, M., Bjornson, K. & Black-Schaffer, A. M. Impurity bound states in fully gapped *d*-wave superconductors with subdominant order parameters. *Sci. Rep.* **7**, 44107 (2017).
- Anderson, P. W. Theory of dirty superconductors. *J. Phys. Chem. Solids* **11**, 26–30 (1959).
- Maier, T. A., Jarrell, M. S. & Scalapino, D. J. Structure of the pairing interaction in the two-dimensional Hubbard model. *Phys. Rev. Lett.* **96**, 047005 (2006).
- Hähner, U. R. et al. DCA++: a software framework to solve correlated electron problems with modern quantum cluster methods. *Comp. Phys. Commun.* **246**, 106709 (2020).
- Chen, K. S. et al. Unconventional superconductivity on the triangular lattice Hubbard model. *Phys. Rev. B* **88**, 041103(R) (2013).

39. Huang, Y. & Sheng, D. N. Topological chiral and nematic superconductivity by doping Mott insulators on triangular lattice. *Phys. Rev. X* **12**, 031009 (2022).
40. Volovik, G. E. On edge states in superconductors with time inversion symmetry breaking. *JETP Lett.* **66**, 522–527 (1997).
41. Laughlin, R. B. Magnetic induction of $d_{x^2-y^2} + id_{xy}$ order in high- T_c superconductors. *Phys. Rev. Lett.* **80**, 5188–5191 (1998).
42. Senthil, T., Marston, J. B. & Fisher, M. P. A. Spin quantum Hall effect in unconventional superconductors. *Phys. Rev. B* **60**, 4245–4254 (1999).
43. Ming, F. F. et al. Hidden phase in a two-dimensional Sn layer stabilized by modulation hole doping. *Nat. Commun.* **8**, 14721 (2017).
44. De Gennes, P. G. Boundary effects in superconductors. *Rev. Mod. Phys.* **36**, 225–237 (1964).
45. Duke, C. B. Semiconductor surface reconstruction: the structural chemistry of two-dimensional surface compounds. *Chem. Rev.* **96**, 1237 (1996).

Publisher's note Springer Nature remains neutral with regard to jurisdictional claims in published maps and institutional affiliations.

Springer Nature or its licensor (e.g. a society or other partner) holds exclusive rights to this article under a publishing agreement with the author(s) or other rightsholder(s); author self-archiving of the accepted manuscript version of this article is solely governed by the terms of such publishing agreement and applicable law.

© The Author(s), under exclusive licence to Springer Nature Limited 2023

Methods

Sample preparation

The hole-doped ($\sqrt{3} \times \sqrt{3}$)-Sn structure was grown on three heavily boron-doped p-type silicon substrates with nominal room-temperature resistivities of 0.002, 0.005 and 0.008 Ω cm. They correspond to surface hole-doping concentrations of 10%, 8% and 6%, respectively, due to differences in the amount of charge transfer from the bulk to the surface¹⁹. These substrates were annealed to 1,200 °C in an ultrahigh vacuum to prepare atomically clean Si surfaces. Sn atoms were deposited onto the clean surface from a thermal effusion cell and the substrate temperature was maintained at around 600 °C. This procedure resulted in the formation of coexisting ($\sqrt{3} \times \sqrt{3}$)-Sn and ($2\sqrt{3} \times 2\sqrt{3}$)-Sn domains. The maximum size (without an internal domain boundary) of the ($\sqrt{3} \times \sqrt{3}$)-Sn superconducting domains on each substrate exceeds 200×200 nm². A small amount of additional Sn atoms are deposited onto the surface when the sample is at 120 K, followed by a fast transfer to the STM measurement stage at a lower temperature. Additional details can be found elsewhere¹⁹.

STM/STS measurements

The STM data were acquired using a cryogenic STM (Unisoku) that can cool the sample and tip to 400 mK in the presence of a perpendicular magnetic field of up to 15 T. Differential conductance spectra dI/dV or their spatial maps $g(\mathbf{r}, V)$ were acquired using lock-in detection with a typical modulation voltage of $V_{r.m.s.} = 0.14$ mV and a typical modulation frequency of 673 Hz. A typical $g(\mathbf{r}, V)$ map consists of 272×272 pixels measured over a 56×56 nm² surface area. The QPI images are then produced by calculating the power spectral density of the Fourier transforms of the real-space conductance map $|g(\mathbf{r}, V)|$.

STS fits

We fit the normalized dI/dV spectra (Fig. 2a) with DOS $N_s(\omega)/N_n(\omega)$, where $N_{s(n)}(\omega) = -\frac{2}{\pi N} \sum_{\mathbf{k}} \text{Im} G_{11}(\mathbf{k}, \omega)$ denotes the DOS in the superconducting (normal) state. Here

$$\hat{G}(\mathbf{k}, \omega) = \frac{(\omega + i\Gamma) \hat{\tau}_0 + \epsilon(\mathbf{k}) \hat{\tau}_3 + \hat{\Delta}(\mathbf{k})}{(\omega + i\Gamma)^2 - \epsilon^2(\mathbf{k}) - |\hat{\Delta}(\mathbf{k})|^2} \quad (1)$$

is the non-interacting Green's function in Nambu space, $\hat{\tau}_\alpha$ are Pauli matrices, $\epsilon(\mathbf{k})$ is the bare-band dispersion and $\hat{\Delta}(\mathbf{k})$ parameterizes the superconducting gap function in Nambu space $\psi_{\mathbf{k}} = [c_{\mathbf{k},\uparrow}, c_{-\mathbf{k},\downarrow}^\dagger]^\top$. Note that for the chiral p -wave case, the space corresponds to the vector $\vec{a} = \hat{z}$.

To model the Sn surface state, we adopted the tight-binding model derived from another work¹⁸, which is derived from ab initio electronic structure calculations. The band dispersion is

$$\begin{aligned} \epsilon(\mathbf{k}) = & -2t_1 \left[\cos(k_x a) + 2 \cos\left(\frac{\sqrt{3}}{2} k_y a\right) \cos\left(\frac{1}{2} k_x a\right) \right] \\ & -2t_2 \left[\cos(\sqrt{3} k_y a) + 2 \cos\left(\frac{3}{2} k_x a\right) \cos\left(\frac{\sqrt{3}}{2} k_y a\right) \right] \\ & -2t_3 \left[\cos(2k_x a) + 2 \cos(k_x a) \cos(\sqrt{3} k_y a) \right] \\ & -4t_4 \left[\cos\left(\frac{5}{2} k_x a\right) \cos\left(\frac{\sqrt{3}}{2} k_y a\right) + \cos(2k_x a) \cos(\sqrt{3} k_y a) \right. \\ & \left. + \cos\left(\frac{1}{2} k_x a\right) \cos\left(3\frac{\sqrt{3}}{2} k_y a\right) \right] \\ & -2t_5 \left[\cos(2\sqrt{3} k_y a) + 2 \cos(3k_x a) \cos(\sqrt{3} k_y a) \right] - \mu \end{aligned} \quad (2)$$

where $t_1 = 52.7$ meV, $t_2 = 0.3881t_1$, $t_3 = 0.1444t_1$, $t_4 = -0.0228t_1$, $t_5 = -0.0318t_1$ and $\mu = -0.017$. Note that we adjusted the chemical potential to put the Van Hove singularity of -7.1 meV below E_F (ref. 19).

To model the normal state, we set $\hat{\Delta}(\mathbf{k}) = 0$. To model an s -wave superconductor, we set $\hat{\Delta}(\mathbf{k}) = \Delta_0 \tau_1$. To model the chiral

p - and d -wave cases, we set $\hat{\Delta}(\mathbf{k}) = \frac{\Delta_l(\mathbf{k})}{2} (\hat{\tau}_1 + i\hat{\tau}_2) + \frac{\Delta_r(\mathbf{k})}{2} (\hat{\tau}_1 - i\hat{\tau}_2)$, where $\Delta_l(\mathbf{k}) = 2\Delta_0 [\beta'_l(\mathbf{k}) + i\beta''_l(\mathbf{k})]$ (ref. 46),

$$\begin{aligned} \beta'_{l=1} &= \sqrt{3} \sin\left(\frac{\sqrt{3}k_y a}{2}\right) \cos\left(\frac{k_x a}{2}\right) \\ \text{and } \beta''_{l=1} &= \sin(k_x a) + \cos\left(\frac{\sqrt{3}k_y a}{2}\right) \sin\left(\frac{k_x a}{2}\right) \end{aligned}$$

for chiral p -wave pairing, and

$$\begin{aligned} \beta'_{l=2} &= \cos(k_x a) - \cos\left(\frac{\sqrt{3}k_y a}{2}\right) \cos\left(\frac{k_x a}{2}\right) \\ \text{and } \beta''_{l=2} &= \sqrt{3} \sin\left(\frac{\sqrt{3}k_y a}{2}\right) \sin\left(\frac{k_x a}{2}\right) \end{aligned}$$

for chiral d -wave pairing. We have also fit the spectra with nematic d -wave order parameters (Supplementary Note 2) and found that they are unable to reproduce the experimental spectra.

We then fit the theoretical DOS to the STS data treating Δ_0 and Γ as fitting parameters. The best fits (Fig. 2a) are obtained with $(\Delta_0, \Gamma) = (1.88, 0.290)$, $(0.76, 0.081)$ and $(0.54, 0.170)$ for the s -, chiral p - and chiral d -wave cases, respectively, in units of millielectronvolts.

QPI calculations

The QPI spectra are calculated using the Born approximation to the T -matrix formalism, with a single point-like potential located at the origin. The Fourier transform of the modulation in the electron density is given by

$$\delta N(\mathbf{q}, \omega) = \frac{1}{N} \sum_{\mathbf{k}} \text{Tr} \left[\frac{1}{2\pi} \text{Im} \{ (\hat{\tau}_0 + \hat{\tau}_3) \hat{G}(\mathbf{k}, \omega) \hat{V} \hat{G}(\mathbf{k} + \mathbf{q}, \omega) \} \right] \quad (3)$$

where $\hat{G}(\mathbf{k}, \omega)$ is the Green's function given by equation (1); \hat{V} is the impurity potential; and $\epsilon(\mathbf{k})$ and $\Delta(\mathbf{k})$ are the bare-band dispersion and superconducting order parameter, respectively. We considered both magnetic ($\hat{V} = V_0 \tau_0$) and non-magnetic ($\hat{V} = V_0 \tau_3$) scatterers, whose strengths are parameterized by V_0 . For the superconducting gap, we considered many different pairing symmetries, as parameterized above (Extended Data Fig. 5).

DFT calculations

Plane-wave DFT calculations were implemented using the QUANTUM ESPRESSO open-source computer code⁴⁷. We have used the Perdew–Burke–Ernzerhof exchange–correlation functional⁴⁸ and the ultrasoft pseudopotentials provided by the code^{49,50}. The energy cutoff for the plane waves is 40 Ry. Although DFT cannot capture the Mott state of the ($\sqrt{3} \times \sqrt{3}$)-Sn system, it accurately captures the ground-state structure⁵¹. We employed a (9×9) supercell with 6 Si layers and 27 Sn adatoms in T_4 positions. In total, there are 594 atoms in the unit cell. To simulate the substitutional Si defect, we replaced one of the 27 Sn adatoms with a Si atom. Based on the experimental results, the interstitial Sn adatom is placed at the centre of an equilateral triangle formed by three adjacent Sn atoms of the original ($\sqrt{3} \times \sqrt{3}$)-Sn surface. Hence, the total number of Sn atoms is 28 (Extended Data Fig. 6). The bottom two Si layers and H layer are fixed in these simulations. The (9×9) first Brillouin zone was sampled with a 2×2 Monkhorst–Pack grid⁵² and the geometry is relaxed until the forces are lower than 0.001 Ry Bohr⁻¹. In the total-energy minimized geometry, the Sn atoms forming the triangle are located -0.2 Å above the atoms of the ($\sqrt{3} \times \sqrt{3}$)-Sn layer. The additional Sn adatom at the centre of the triangle is located -0.11 Å above the ($\sqrt{3} \times \sqrt{3}$)-Sn layer, that is, -0.09 Å below its nearest neighbours.

STM image simulations

The simulated STM images for both defect structures were calculated using the Keldysh–Green function formalism⁵³ together with the FIREBALL local-orbital DFT Hamiltonian⁵⁴. This procedure has

been successfully used in many works before⁵⁵. In our simulations, a standard W tip is placed at a distance of 5 Å above the surface, and images were generated for tunnelling parameters close to the experimental conditions. In Extended Data Fig. 6, we show the experimental and simulated images side by side, showing excellent agreement for the chosen tunnelling parameters. The STM images can be correlated to the different atomic heights and the projected DOS on different atoms. The projected DOS on the interstitial Sn adatom, calculated with the local-orbital DFT code, is shown in Extended Data Fig. 6. A similar procedure was implemented for the substitutional Si defect. The corresponding experimental and theoretical images are shown in Extended Data Fig. 6 and are in good agreement.

DCA calculations

DCA calculations for the triangular-lattice single-band Hubbard model were performed with the DCA++ package³⁷ using a continuous-time quantum Monte Carlo impurity solver. Here we consider an $N = 3 \times 3$ cluster of Sn atoms with the bare-band structure given elsewhere¹⁸ but including only up to the third-nearest-neighbour hopping (that is, $t_4 = t_5 = 0$), since the cluster cannot support longer-range hopping. We further set $U = 0.66$ eV (ref. ¹⁸). The DCA calculations measured the single-particle Green's function and two-particle Green's function in the particle-particle channel with zero momentum and frequency transfer. Consequently, we extracted the irreducible particle-particle vertex and then solved the Bethe–Salpeter equation to obtain the leading eigenvalues and eigenvectors in the particle-particle channel³⁶. The pairing symmetry of the dominant superconducting instability can be extracted from the leading eigenvector.

Edge-state calculations

We compute the topological edge states of the chiral $d + id$ superconductor by solving the same triangular-lattice model defined in equation (2) but defined on a cluster with open-boundary conditions in the y direction and periodic boundary condition in the x direction (Extended Data Fig. 10). Introducing the labels m and n for the chains stacked in the y direction and k for the momentum along the edge, the Hamiltonian can be written as

$$H = \frac{1}{2} \sum_{mn} \sum_k \Phi_m^\dagger(k) \mathcal{H}_{mn}(k) \Phi_n(k) \quad (4)$$

where $\Phi_n^\dagger(k) = [c_{n1}^\dagger(k), c_{n1}(-k)]$ is a Nambu spinor collecting electron and hole degrees of freedom. The Hamiltonian matrix \mathcal{H}_{mn} describes how the chains m and n are coupled. It is convenient to decompose \mathcal{H}_{mn} (momentum dependence is suppressed) as

$$\mathcal{H}_{mn} = \sum_{p=-l}^l \mathcal{H}_p \delta_{p,n-m} \quad (5)$$

where \mathcal{H}_p captures the coupling of the $|p|$ th-nearest-neighbour chains and satisfies $\mathcal{H}_{-p} = \mathcal{H}_p^\dagger$. Here l denotes the extent of coupling; if only the first-nearest-neighbour chains are coupled, then $l = 1$. In the present problem, $l = 4$. The matrices \mathcal{H}_p are given by

$$\mathcal{H}_p = \begin{pmatrix} \epsilon_p & \Delta_p \\ \Delta_p^\dagger & -\epsilon_p \end{pmatrix} \quad (6)$$

The Hamiltonian defines a Schrödinger equation given by

$$\sum_{p=-4}^4 \mathcal{H}_p(k) \Psi_{n+p}(k) = E \Psi_n(k) \quad (7)$$

where $\Psi_n(k) = [u_n(k), v_n(k)]^T$ is the wave function with electron and hole components $u_n(k)$ and $v_n(k)$, respectively. We numerically solve this system of equations on a finite slab to obtain the quasiparticle

spectrum E_k^ξ in the presence of an edge. Here ξ is an index to label the eigenvalues at a given k . For a system with N chains, one has $\xi = 1, \dots, 2N$.

Finally, we compute the chain-resolved local DOS $N(n, \omega)$ as

$$N(n, \omega) = \sum_{k, \xi} |u_n^\xi(k)|^2 \delta(\omega - E_k^\xi) + |v_n^\xi(k)|^2 \delta(\omega + E_k^\xi) \quad (8)$$

Data availability

The data supporting this study are available via Zenodo at <https://doi.org/10.5281/zenodo.7249821>.

Code availability

The DCA++ code used for this project is available via GitHub at <https://github.com/CompFUSE/DCA>. The QUANTUM ESPRESSO code can be obtained from <https://www.quantum-espresso.org/>. The FIREBALL code is available via GitHub at <https://github.com/fireball-QMD>. Codes for performing the QPI and edge-state calculations are available via Zenodo at <https://doi.org/10.5281/zenodo.7249821>.

References

- Zhou, S. & Wang, Z. Nodal $d + id$ pairing and topological phases on the triangular lattice of $\text{Na}_x\text{CoO}_2 \cdot y\text{H}_2\text{O}$: evidence for an unconventional superconducting state. *Phys. Rev. Lett.* **100**, 217002 (2008).
- Giannozzi, P. et al. QUANTUM ESPRESSO: a modular and open-source software project for quantum simulations of materials. *J. Phys.: Condens. Matter* **21**, 395502 (2009).
- Perdew, J. P., Burke, K. & Ernzerhof, M. Generalized gradient approximation made simple. *Phys. Rev. Lett.* **77**, 3865–3868 (1996).
- Goedecker, S., Teter, M. & Hutter, J. Separable dual-space Gaussian pseudopotentials. *Phys. Rev. B* **54**, 1703–1710 (1996).
- Hartwigsen, C., Goedecker, S. & Hutter, J. Relativistic separable dual-space Gaussian pseudopotentials from H to Rn. *Phys. Rev. B* **58**, 3641–3662 (1998).
- Pérez, R., Ortega, J. E. & Flores, F. Surface soft phonon and the $(d_{x^2-y^2} + id_{xy}) \leftrightarrow (3 \times 3)$ phase transition in Sn/Ge(111) and Sn/Si(111). *Phys. Rev. Lett.* **86**, 4891–4894 (2001).
- Monkhorst, M. J. & Pack, J. D. Special points for Brillouin-zone integrations. *Phys. Rev. B* **13**, 5188–5192 (1976).
- Blanco, J. M. et al. First-principles simulations of STM images: from tunneling to the contact regime. *Phys. Rev. B* **70**, 085405 (2004).
- Lewis, J. P. et al. Advances and applications in the FIREBALL ab initio tight-binding molecular-dynamics formalism. *Phys. Status Solidi B* **248**, 1989–2007 (2011).
- González, C. et al. Formation of atom wires on vicinal silicon. *Phys. Rev. Lett.* **93**, 126106 (2004).
- Ming, F., Smith, T. S., Johnston, S., Snijders, P. C. & Weitering, H. H. Zero-bias anomaly in nanoscale hole-doped Mott insulators on a triangular silicon surface. *Phys. Rev. B* **97**, 075403 (2018).

Acknowledgements

We thank C. D. Batista, P. J. Hirschfeld, P. Kent, A. Tennant and R. Zhang for fruitful discussions. The experimental work and QPI calculations were supported by the Guangdong Basic and Applied Basic Research Foundation (ref no. 2021A1515012034) and by the Office of Naval Research under grant no. N00014-18-1-2675. F.M. acknowledges support from the NSFC (no. 12174456) and the Guangdong Basic and Applied Basic Research Foundation (grant no. 2020B1515020009). C.G. acknowledges financial support from the Community of Madrid through the project NANOMAGCOST CM-PS2018/NMT-4321 and the computer resources at Centro de Computación Científica at UAM (project Biofast) as well as Altamira, with the technical support provided by the Instituto de Física de Cantabria (IFCA) via project QHS-2021-3-0005. J.O. acknowledges financial support by the

Spanish Ministry of Science and Innovation through grants MAT2017-88258-R and CEX2018-000805-M (María de Maeztu Programme for Units of Excellence in R&D). The DCA calculations were supported by the Scientific Discovery through Advanced Computing (SciDAC) program funded by the US Department of Energy (DOE), Office of Science, Advanced Scientific Computing Research, and Basic Energy Sciences, Division of Materials Sciences and Engineering. This research also used resources of the Oak Ridge Leadership Computing Facility, which is a DOE Office of Science User Facility supported under contract DE-AC05-00OR22725.

Author contributions

F.M. and X.W. contributed equally to this work. F.M., X.W., C.C. and K.D.W. prepared the samples and performed the STM experiments. P.M. and T.A.M. performed the DCA calculations. J.S. and J.W.F.V. performed the edge-state calculations. C.G. and J.O. performed the DFT calculations and STM image simulations. S.J. performed the QPI calculations. S.J. and H.H.W. conceived and supervised the project and wrote the manuscript with input from all the authors.

Competing interests

The authors declare no competing interests.

Additional information

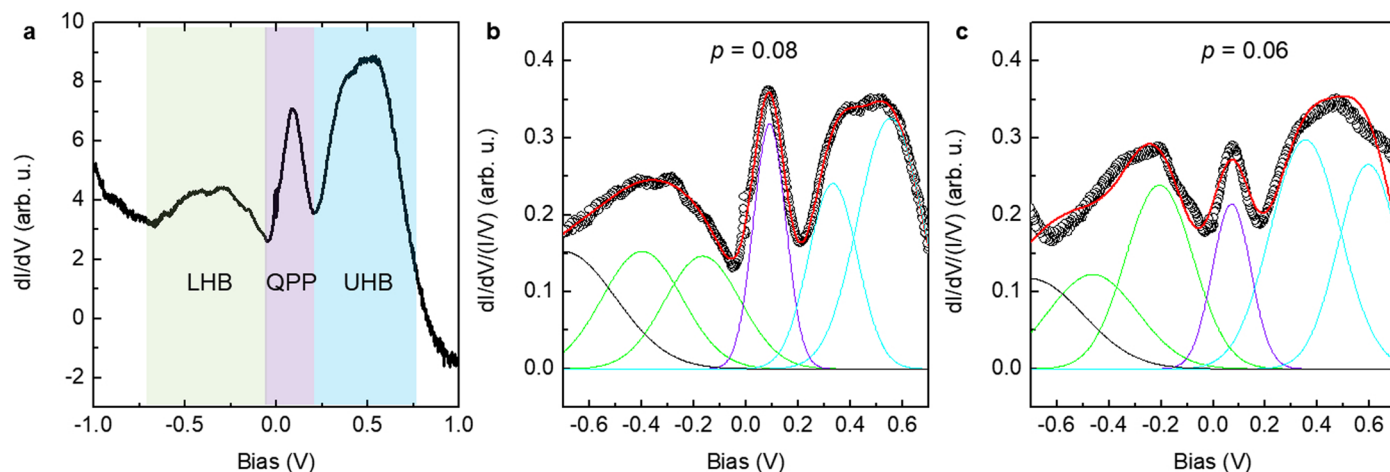
Extended data is available for this paper at <https://doi.org/10.1038/s41567-022-01889-1>.

Supplementary information The online version contains supplementary material available at <https://doi.org/10.1038/s41567-022-01889-1>.

Correspondence and requests for materials should be addressed to K. D. Wang, S. Johnston or H. H. Weitering.

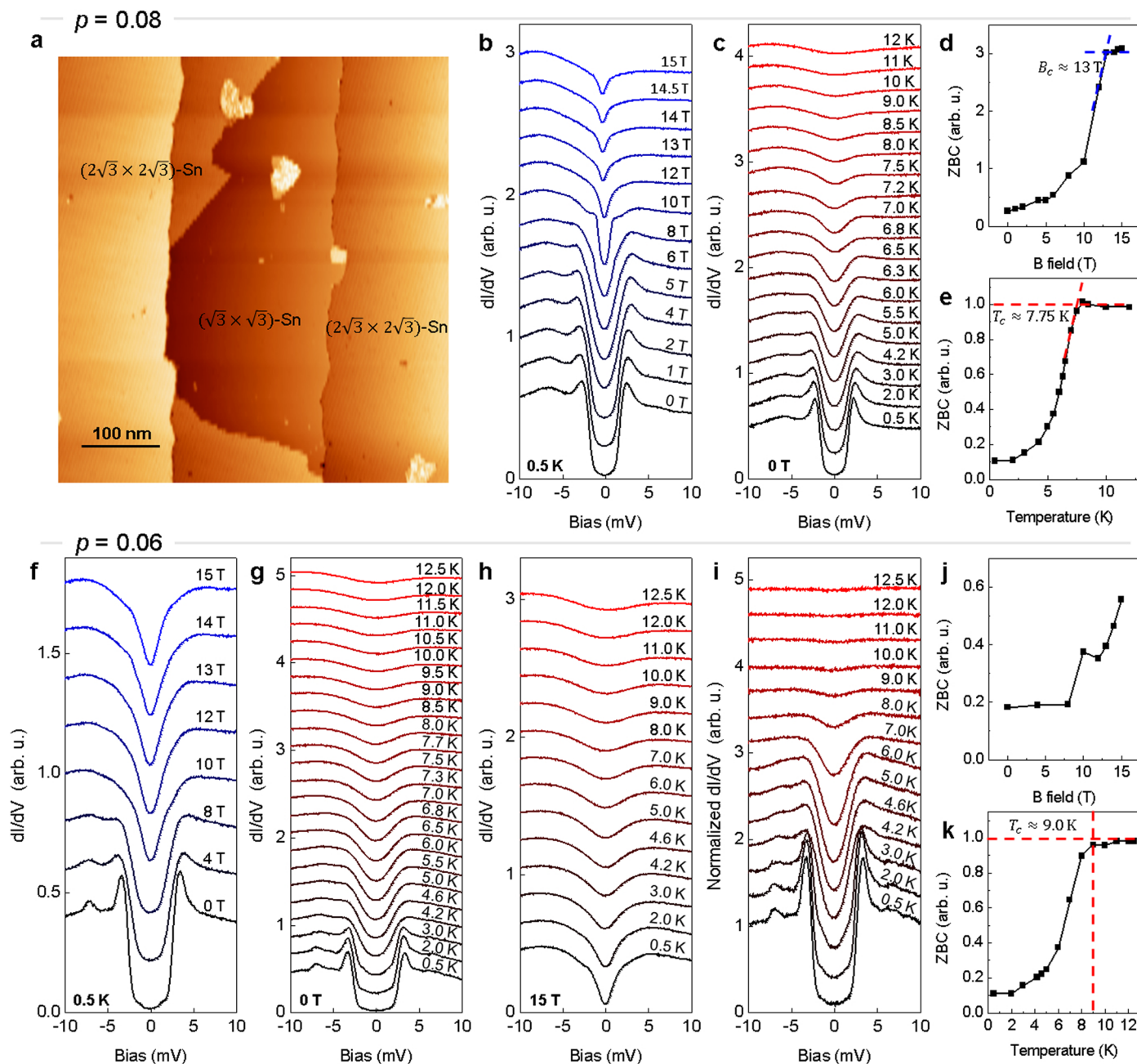
Peer review information *Nature Physics* thanks the anonymous reviewers for their contribution to the peer review of this work.

Reprints and permissions information is available at www.nature.com/reprints.



Extended Data Fig. 1 | Spectral features of the $(\sqrt{3} \times \sqrt{3})$ -Sn surface grown on two different Si wafers and estimates of the hole concentration. **a dI/dV spectrum of the $p = 0.08$ surface at 0.5 K, featuring the lower Hubbard band, quasi-particle peak, and upper Hubbard band (LHB/QPP/UHB). **b** $dI/dV/(I/V)$ spectrum obtained from the spectrum in panel a, fitted with six Gaussian peaks. From the fitting, we find that the area under the QPP represents 16.1% of the total spectrum, excluding the peak on the far left which represents the contribution of**

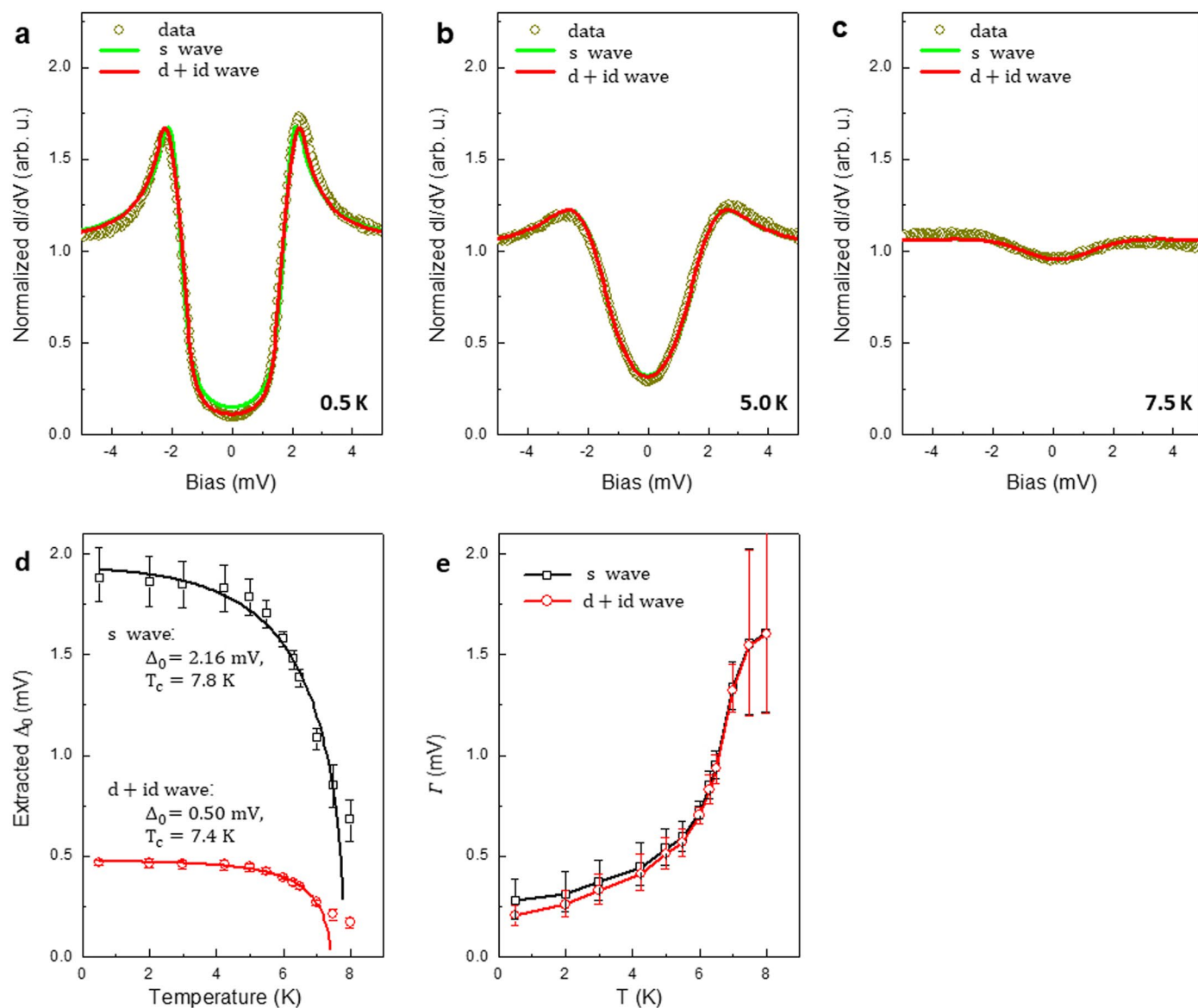
the silicon valence band. This area fraction converts to a hole doping level of 8.05%, i.e., $p = 0.08$; See Ref.¹⁸ for more details. **c** $dI/dV/(I/V)$ spectrum of the $(\sqrt{3} \times \sqrt{3})$ -Sn surface (0.5 K), subject to the same fitting analysis as in **b**. The area fraction of the QPP is 12.1%, which corresponds to hole doping level of 6.05% ($p = 0.06$). Gaussians are used only for the purpose of spectral area determination.



Extended Data Fig. 2 | Tunneling spectroscopy of the superconducting state.

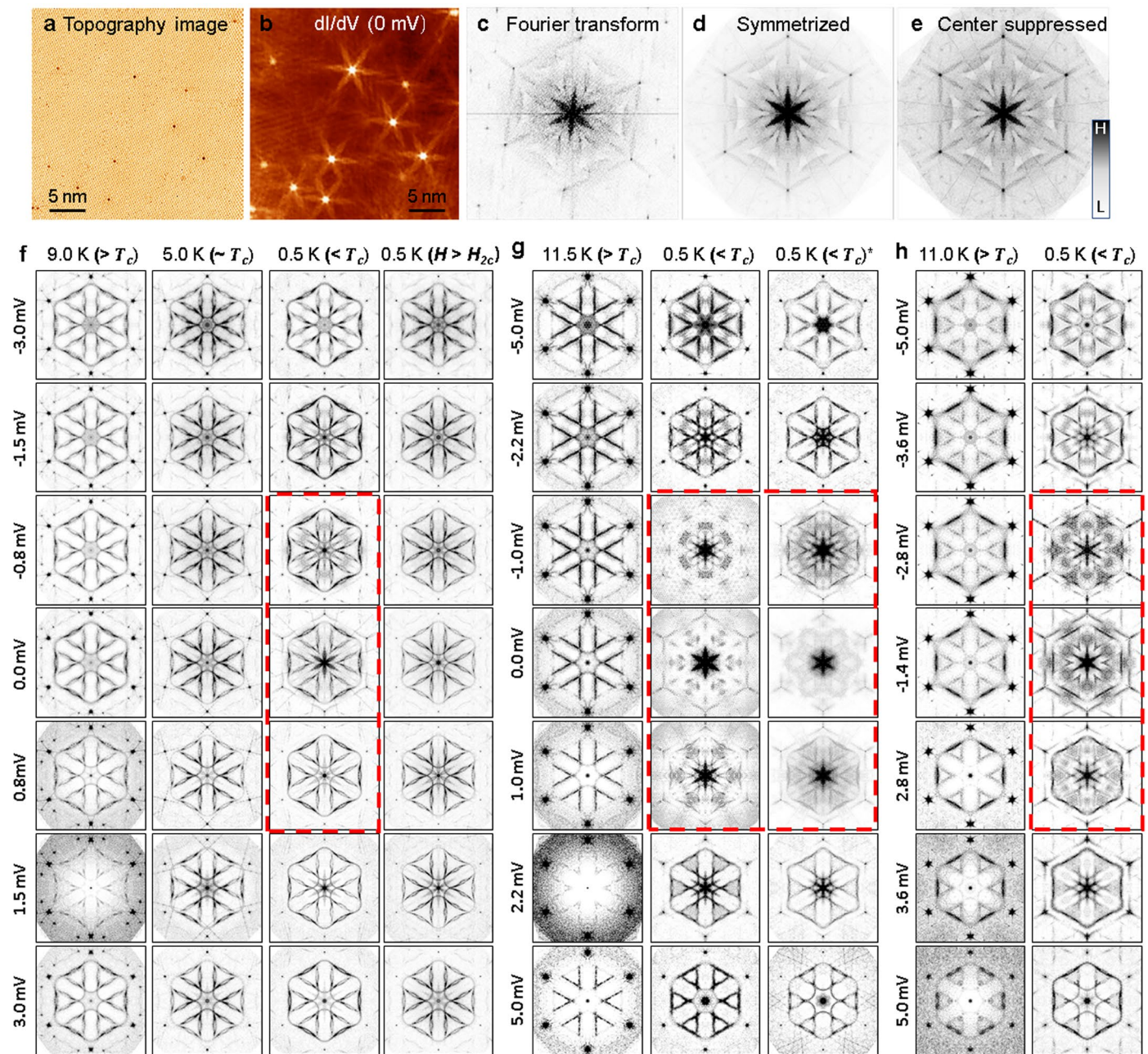
a STM image ($V_s = -2$ V, $I_t = 0.01$ nA) of the $p = 0.08$ surface with neighbouring (competing) $(\sqrt{3} \times \sqrt{3})\text{-Sn}$ and $(2\sqrt{3} \times 2\sqrt{3})\text{-Sn}$ domains. The former is superconducting while the latter is semiconducting. **b–e** STM tunneling spectra of the superconducting phase for $p = 0.08$. **b**, Field dependent dI/dV spectra measured at 0.5 K. **c**, Temperature dependent dI/dV spectra measured in zero B-field. **d**, Zero bias conductance (ZBC) extracted from panel **b**. The ZBC increases with the B field and saturates at ~ 13 T. **e**, ZBC extracted from normalized dI/dV (most of the data are shown in Fig. 1e). The ZBC increases with the temperature and saturates around 7.8 K. **f–k** Tunneling spectra from the $p = 0.06$ surface. **f**, Field dependent dI/dV spectra measured at 0.5 K. **g**, Temperature dependent dI/dV spectra measured in zero B-field. **h**, Temperature dependent dI/dV spectra

measured in at 15 T. **i**, dI/dV spectra normalized by dividing the spectra in panel **g** with the corresponding spectra in panel **h** (same temperature), except for the 0.5 K and 2.0 K data in panel **g**, for which we used the 3.0 K data in panel **h** so as to avoid division by the very small signal at zero bias. Note the persistence of the gap feature up to 9 K. **j**, ZBC extracted from panel **f**. The ZBC increases with the B-field and does not saturate at 15 T. **k**, ZBC extracted from panel **i**. The ZBC increases with temperature and saturates around 9 K. The normal state spectra in **b** and **c** exhibit minor suppression of the conductance near zero bias, which is due to the slow dissipation of the tunneling charge from the surface into the bulk, see Ref. ⁵⁶ for more details. Such effect becomes more significant for the $p = 0.06$ sample in panel **f–g**.



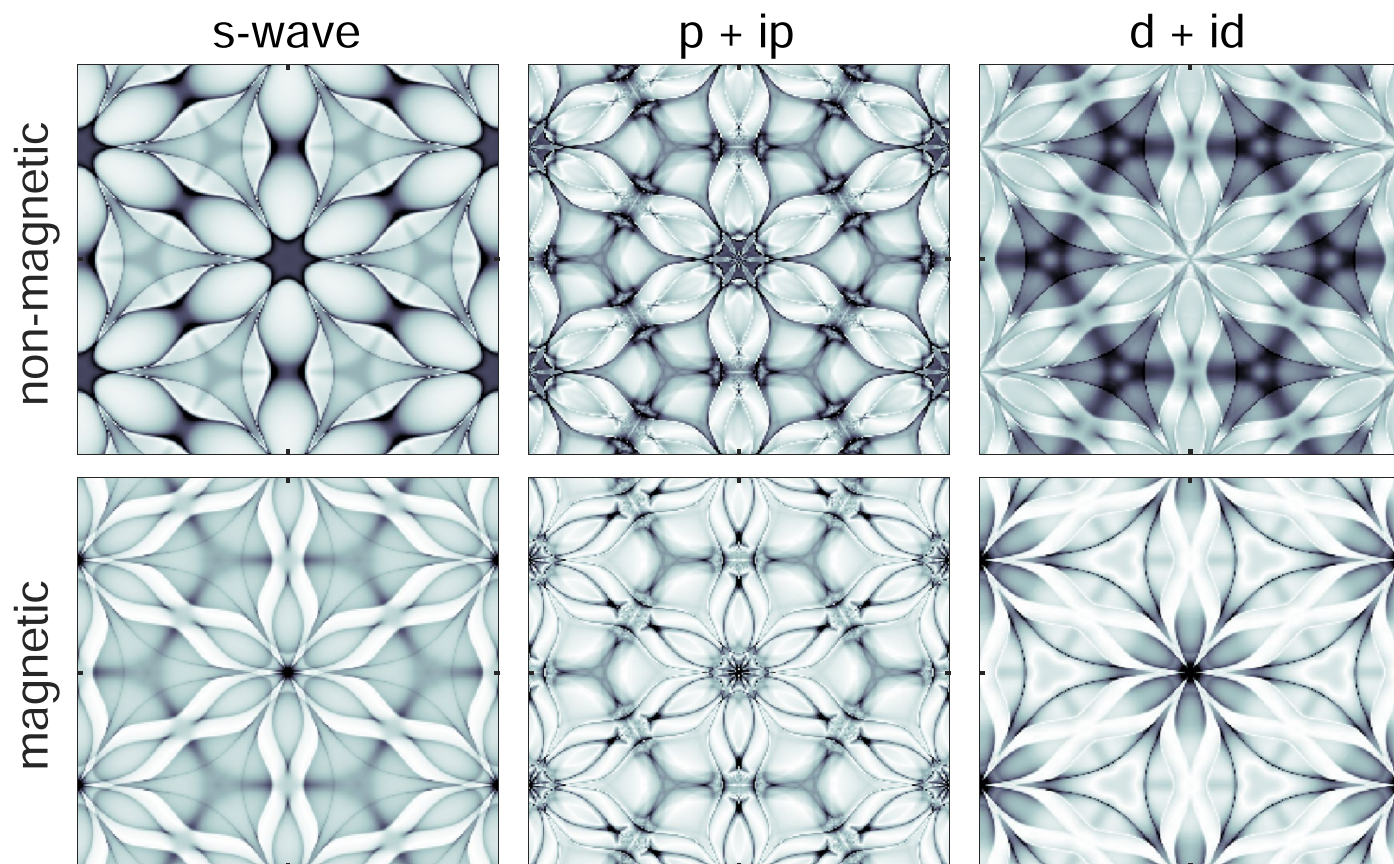
Extended Data Fig. 3 | Fitting of the tunneling spectra. To fit the full T -dependence, we performed a Dynes-like fit of the dI/dV spectra while adopting an angular-dependent gap function $\Delta(\theta)$ as parameterized in Ref. ¹⁶. (The results obtained using this approach are consistent with those obtained by fitting the full momentum-dependence Green's function in the superconducting state,

see Fig. 2.) **a–c** Fitting results for the $p = 0.08$ system, assuming s -wave and $d_{x^2+y^2} + id_{xy}$ order parameters. The s -wave and $d_{x^2+y^2} + id_{xy}$ -wave fits only reveal minor differences. **d** Extracted values of Δ_0 as a function of temperature. **e** The corresponding temperature dependence of the broadening parameter Λ . Error bars in **d** and **e** are estimated in a way similar to Ref. ¹⁶.



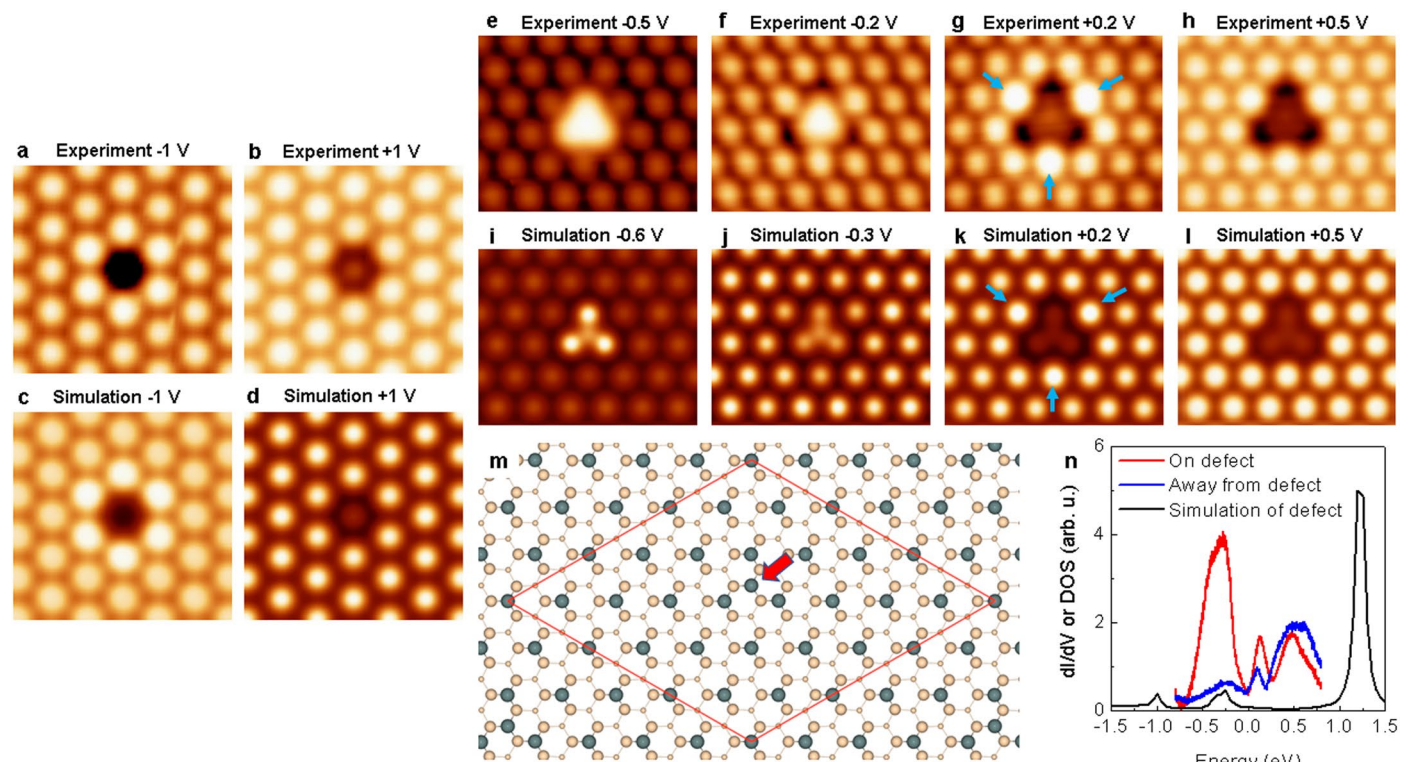
Extended Data Fig. 4 | Experimental QPI results. **a–e** QPI data and processing procedures. **a** STM image ($V_s = 0.1$ V, $I_t = 0.1$ nA) of a $(\sqrt{3} \times \sqrt{3})$ -Sn surface ($p = 0.1$) with several surface defects appearing as dark spots. **b** Corresponding dI/dV image at $T = 0.5$ K. The bright star-like features are centered at the defect locations in panel **a**. **c** The power spectrum of panel **b**, symmetrized and rotated in panel **d**. The central region is subsequently suppressed to enhance the high frequency features, as shown in panel **e** [see Ref. ¹⁸ for more details]. **f–h** show 4, 3, and 2 sets of QPI results obtained from $(\sqrt{3} \times \sqrt{3})$ -Sn surfaces for $p = 0.1, 0.08$, and 0.06 , respectively. Each column shows QPI images obtained in a fixed spatial region but with different biases, as indicated on the left. The measurement temperatures are labeled above each column, and data are shown for

temperatures above and below T_c . The central flower leaves only appear when the sample is in superconducting state and when the measurement bias is within the superconducting gap (within ± 1.5 mV, ± 2.2 mV, and ± 3.6 mV, in **f**, **g**, and **h**, respectively). These QPI images are enclosed by the dashed red rectangles. Panel **f** shows QPI results obtained at $T = 5$ K (slightly larger than $T_c = 4.7$ K for this sample), or at 0.5 K in an 8 T B-field ($H_{2c} = 3$ T). These data have a significantly reduced flower leaf feature, which could come from superconducting fluctuations. In panel **g**, the “0.5 K ($< T_c$)*” data are QPI results obtained from a sample with interstitial Sn adatoms, deposited at 120 K. The presence of interstitial Sn considerably enhances the flower-leaf features at the center of the Brillouin zone.



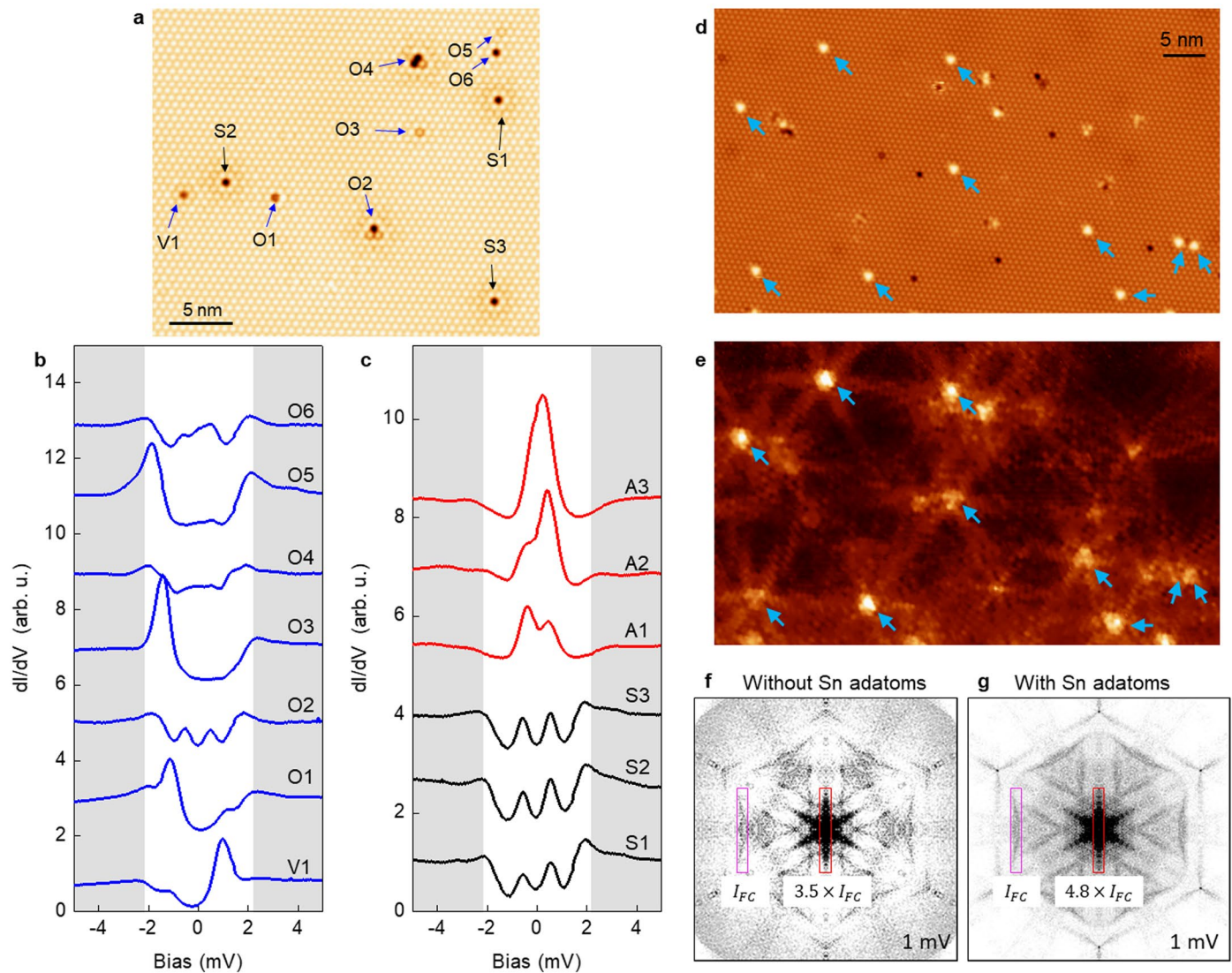
Extended Data Fig. 5 | Simulated QPI spectra for different gap symmetries and scattering centers. The top and bottom rows show results for nonmagnetic ($\hat{V} = V_0 \hat{\tau}_3$) and magnetic ($\hat{V} = V_0 \hat{\tau}_0$) scatterers, respectively, with $V_0 = 100$ meV. Results are shown in the superconducting state assuming s-wave (left column), chiral $p + ip$ (middle column), and $d + id$ (right column) order parameters.

The spectra are calculated at a bias voltage of 1 meV. In each case, the magnitude of the gap Δ_0 and smearing parameter δ are obtained from fits of the dI/dV spectra shown in Fig. 2a (see Methods). Note the absence of the central flower-leaf feature for non-magnetic scattering combined with the s-wave order parameter.



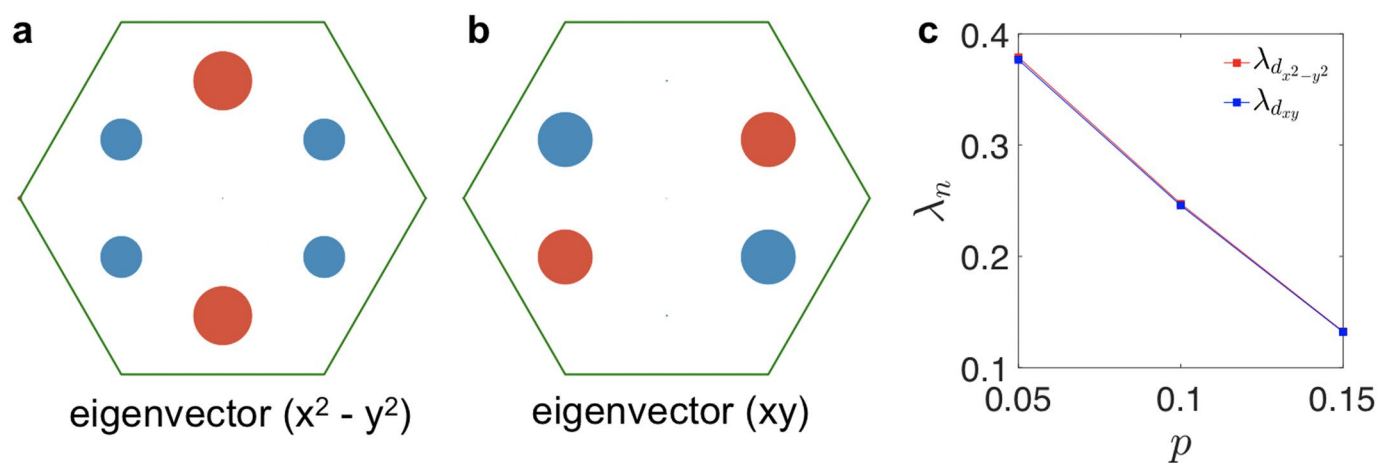
Extended Data Fig. 6 | Experimental and simulated STM images of the substitutional Si and interstitial Sn adatom defects. **a–d** Experimental ($I_t = 0.1$ nA) and simulated STM images for the substitutional Si defect. The Si atom is invisible in filled state images, indicating that there are no occupied dangling bond states to tunneling from. The Si atom is visible in empty state images, but the atom appears to be dim due to its smaller covalent radius. **e–h** Experimental STM images ($I_t = 0.1$ nA) of the interstitial Sn adatom defect center. Panel **e** reveals three very bright adatoms that are part of the regular $(\sqrt{3} \times \sqrt{3})$ -Sn lattice. The interstitial Sn atom is located at the center of this cluster and cannot be imaged within the accessible bias range, as the adatom moves at higher biases. **i–l** Simulated STM images. Note the slightly increased brightness of the Sn atoms indicated by the blue arrows in panel **g**. This subtle

effect is captured by the theory simulation in panel **k**. **m** (9×9) supercell used in the DFT calculations for the interstitial Sn adatom defect. Sn adatom and Si substrate atoms are shown in green and gold, respectively. The interstitial Sn atom is placed near the center of the (9×9) unit cell, as indicated by the red arrow. **n** Experimental dI/dV spectra recorded on top of the interstitial adatom (red) and far away from the interstitial location (blue). The latter reveals the characteristic LHB/QPP/UHB features (see Extended Data Fig. 1). The strong peak at about -0.35 eV corresponds to the triangular adatom feature in panels **a**, **e**. It is captured by the DFT calculation (black line). The peak at +1.25 eV in the theoretical DOS mainly consists of the (empty) $5p$ orbitals of the interstitial adatom. Simulated images at this bias indeed visualize this atom (not shown), but it cannot be imaged at this tunneling bias.



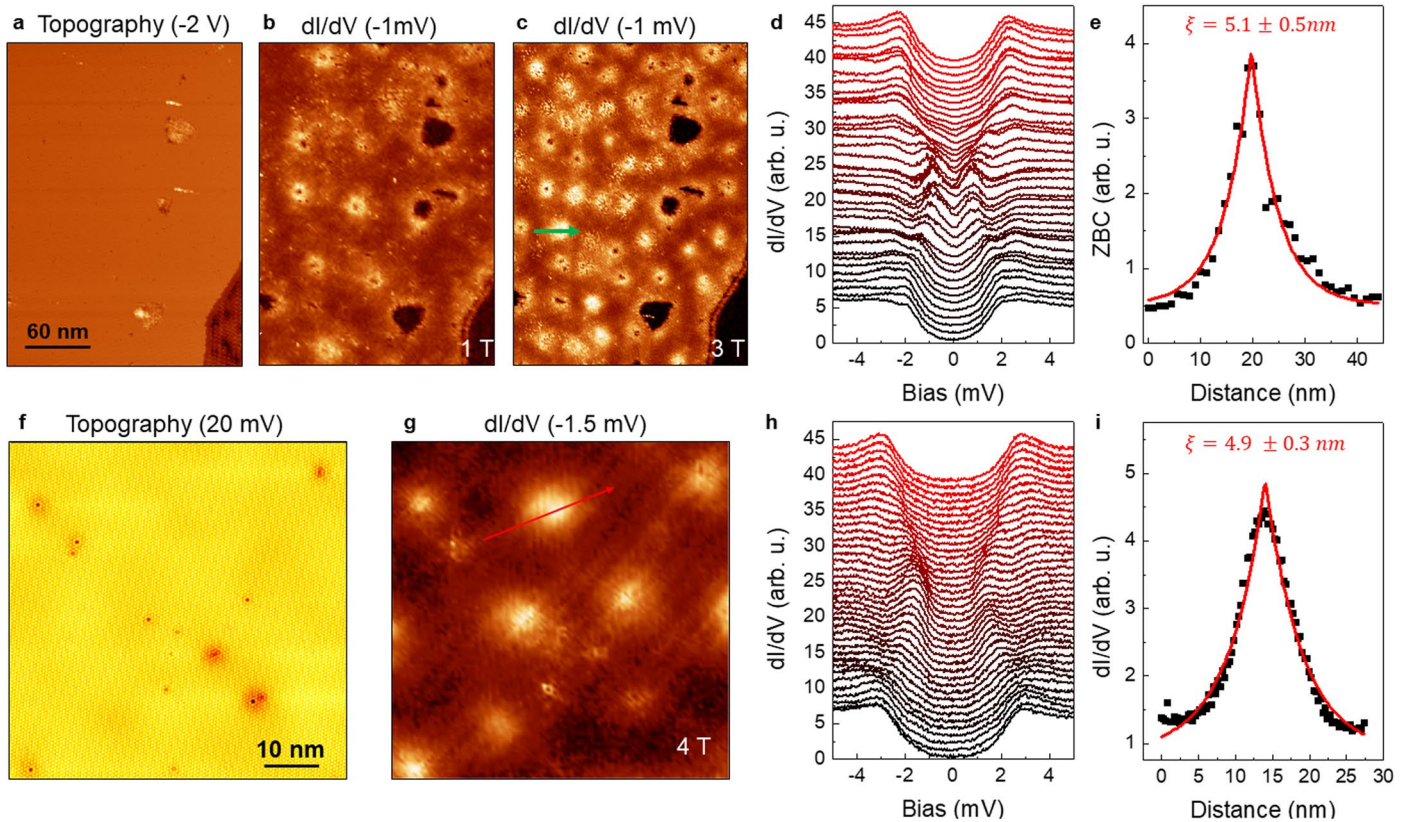
Extended Data Fig. 7 | Tunneling spectra (0.5 K) measured at defect locations on the superconducting ($\sqrt{3} \times \sqrt{3}$)-Sn surface ($p=0.08$) and corresponding QPI data. **a STM image ($V_s = 0.02$ V, $I_t = 0.1$ nA) showing several intrinsic surface defects. S1, S2 and S3 are substitutional Si defects and V1 is a Sn vacancy, as judged by the appearance of a hole for a wide range of positive and negative tunneling biases (images at other biases are not shown). Defects with unknown structures are labelled On, with $n = 1 - 6$. **b** Tunneling spectra of the V1 and On defects in panel **a**. **c** Tunneling spectra of the interstitial Sn adatom defects A1, A2, and A3; see Supplementary Fig.. All defects produce a pair of in-gap states. The substitutional Si defects (S1, S2, and S3) exhibit a well defined double-peak structure at ± 0.6 meV. Interstitial Sn adatoms (A1 and A2) also possess a double peak structure, but with smaller energy splitting (± 0.2 meV). The A3 defect appears to have a single (unresolved) peak structure. **d** STM image ($V_s = -0.5$ V,**

$I_t = 0.1$ nA) of a the ($\sqrt{3} \times \sqrt{3}$)-Sn surface with interstitial Sn defects (indicated by arrows) and other intrinsic defects, mostly substitutional Si or adatom vacancies. **e** Corresponding dI/dV image obtained at a sample bias of $V_s = -0.4$ mV. The interstitial Sn defects produce the strongest scattering features in the real space conductance maps, as compared to those of other intrinsic defects. **f, g** compares the QPI spectra from the same ($\sqrt{3} \times \sqrt{3}$)-Sn surface with and without adsorbed Sn defects. I_{FC} represents averaged scattering intensities for the segment of the Fermi contour enclosed by the magenta rectangle, while the averaged intensity for the flower leaf features near the center of the Brillouin zone (enclosed by the red rectangle) is represented in units of I_{FC} . The relative scattering intensity of the flower leaf feature is strongest for the surface with the interstitial Sn adatoms defects.



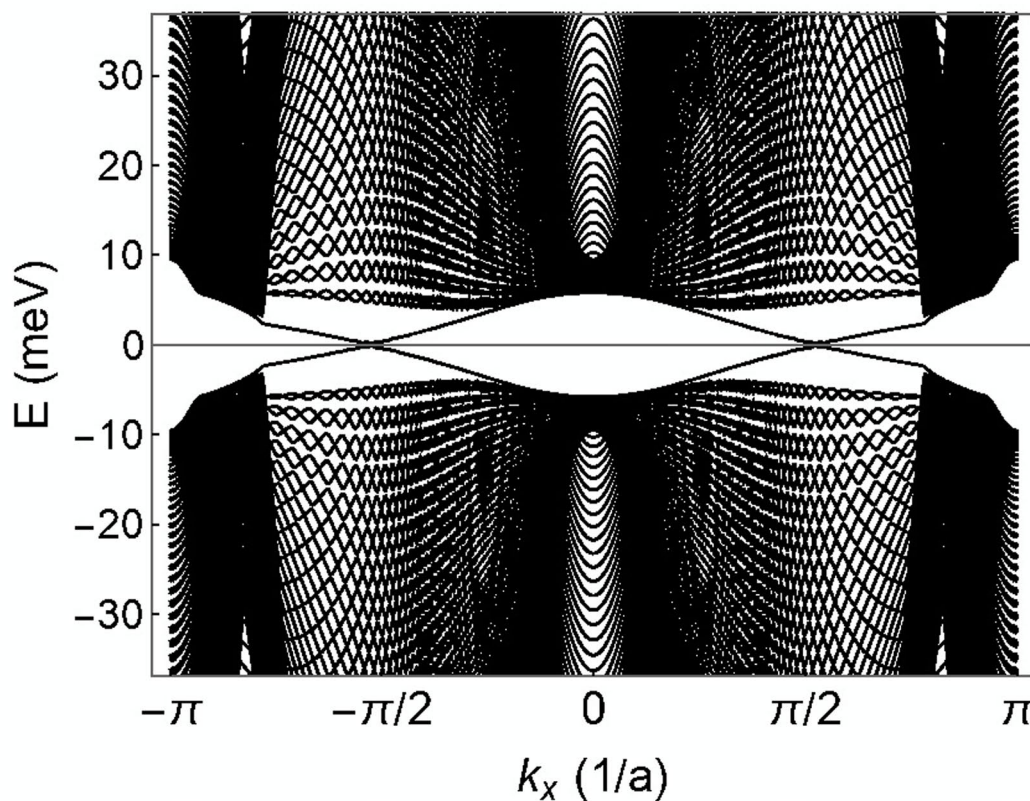
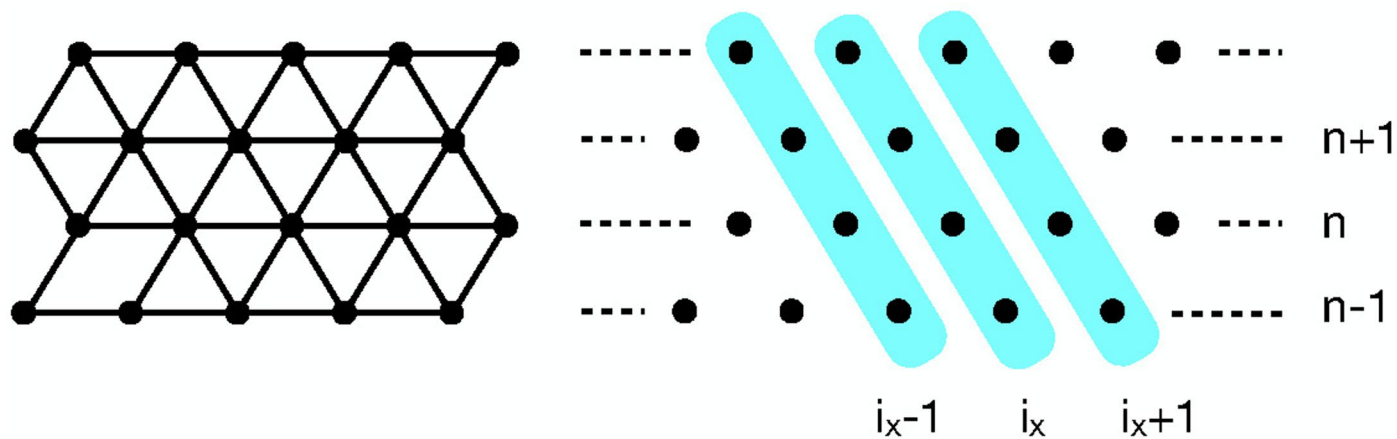
Extended Data Fig. 8 | The leading (degenerate) eigenvectors of the Bethe-Salpeter equation for the triangular lattice Hubbard model. a, b The momentum space structure of the leading eigenvectors, which show a pairing symmetry consistent with $d_{x^2-y^2} + id_{xy}$ pairing. The size and color of the dots

indicate the magnitude and sign of the eigenvector at the momentum points of the 3×3 cluster. The green hexagon shows the boundaries of the first Brillouin zone. **c** The doping dependence of the leading eigenvalues at an inverse temperature of $\beta = 8/t$.



Extended Data Fig. 9 | Magnetic vortices of the superconducting ($\sqrt{3} \times \sqrt{3}$)-Sn surface observed at 0.5 K. a–e Magnetic vortices for the $p = 0.08$ sample. **a** Topographic STM image. **b, c** dI/dV maps obtained with a tunneling bias inside the superconducting gap with a B-field of 1 T and 3 T, respectively. **d** dI/dV spectra measured along the line crossing a magnetic vortex in panel **c**. **e** ZBC obtained from panel **d** with an exponential fit for determining the superconducting coherence length ξ . **f–i** Magnetic vortices for the $p = 0.06$ sample. **f** Topographic

image. **g** dI/dV map obtained with a tunneling bias inside the superconducting gap with a B-field of 4 T. This sample exhibits a very low zero bias dI/dV signal, presumably due to the very high series resistance of this lightly doped sample at 0.5 K. Therefore the vortex features are only resolved away from zero bias. **h** dI/dV spectra measured along the line crossing a magnetic vortex in panel **g**. **i** dI/dV (~ 1.5 mV) along the line indicated in panel **g** with an exponential fit for determining the superconducting coherence length.



Extended Data Fig. 10 | Electronic band dispersion for a chiral d -wave superconductor in the presence of edges. Results were obtained by considering a mean-field $d_{x^2-y^2} + id_{xy}$ order parameter on a triangular lattice. The edge state spectrum is obtained by solving the tight-binding Hamiltonian on a cylinder, with open boundary conditions along the y -direction and periodic boundary conditions along the x -direction. Momentum k_x remains a good

quantum number and the resulting spectrum is shown here for a system of 400 chains (labeled by n) stacked in the y direction and a k -mesh of 400 points. To clearly show the edge states here we computed the spectrum for $\Delta_0 = 1.5$ meV. As expected for a chiral d -wave superconductor with Chern number $C = \pm 2$, two chiral linearly dispersing in-gap states exist on each edge.